LARGE LOCA BEAU ANALYSIS OF A GENERIC 900MW CANDU PLANT

LARGE LOCA BEAU ANALYSIS OF A GENERIC 900MW CANDU PLANT

BY

POUYA SABOURI

A THESIS
SUBMITTED TO THE DEPARTMENT OF ENGINEERING PHYSICS
AND THE SCHOOL OF GRADUATE STUDIES
OF MCMASTER UNIVERSITY
IN PARTIAL FULFILMENT OF THE REQUIREMENTS
FOR THE DEGREE OF
MASTER OF APPLIED SCIENCE

Master of Applied Science (2010)	McMaster University
(Engineering Physics)	Hamilton, Ontario, Canada

TITLE: Large LOCA BEAU Analysis of a Generic 900MW CANDU Plant

AUTHOR: Pouya Sabouri

SUPERVISOR: Dr. David Novog

NUMBER OF PAGES: iii, 114

Abstract

A RELAP5 input model representative of a 900 MW CANDU plant was created. Due to the one dimensional nature of the code, complex plant components such as heat transport system pumps, fuel channels, and the reactor core were modeled using thermal hydraulically equivalent geometries. The model consists of 301 thermal hydraulic components and heat structures with five boundary conditions specifying the pressure, temperature, and in some cases the mass flow. Spacial convergence of the model was ensured through the implementation of various channel nodalizations (6, 12 and 24 axial nodes) and core representations (single channel group and 6 channel groups per core pass). A control subroutine representative of the pressure control system and steam generator control system was implemented in the model, mimicking the controllers that exist in operational CANDU Reactors. A point kinetics model was used to simulate the reactor power.

Uncertainties for parameters related to the modeling of specific phenomenons were obtained from literature sources related to the models in which the parameters belong to. Where sources of open literature were unavailable (error in the void reactivity coefficient, and trip delay times), an estimate was made for the parameter uncertainties. Uncertainties for plant specific parameters were derived from plant operating data obtained either from plant instrument measurements (RIH pressure, RIH temperature, etc) or through code simulation(channel powers, bundle powers, etc).

Breaks in the NW reactor inlet header were considered. Due to the additional flow

from the pressurizer present in the east loop, it was found that breaks in this loop would lead to slightly lower results. The bulk net energy deposition (NED) related to expected maximum sheath temperatures, and the reactor peak power related to the fuel heat up rate were chosen as the figures of merit. Breaks with a size of 48% of the reactor inlet header area were found to lead to the highest NED. From parametric sensitivity studies performed at the best estimate and non best estimate points for the 48% break, a Phenomena and Key Parameter Identification and Ranking Table(PKPIRT) was established with the void reactivity feed back identified as the highest ranked parameter. It was found that the ranking based on best estimate local studies does not reject parameters that may be of importance at their 95th percentile(non best estimate point).

Two best estimate methods along with a conservative approach were implemented. A brute force monte-carlo method consisting of 10,000 simulations provided a probability distribution function for the figures of merits. First and second order GRS methods were found to adequately predict an upper bound for the 95th percentile of the FOMs. Both best estimate methods demonstrated that the consequences of a hypothetical large break LOCA are much more benign than those predicted by the LOE approach.

Acknowledgements

I wish to thank my supervisor Dr. Novog for his guidance, encouragements and great patience. I also wish to thank Dr. John Luxat for providing the input files from which much of my work was derived from.

Notation and abbreviations

A	pipe flow area or heat transfer area
c_p	specific heat
D	pipe diameter or equivalent heated diameter
f	friction parameter
f_{TP}	two phase friction factor
G	mass velocity
g	acceleration due to gravity
h	heat transfer coefficient or enthalpy
K	junction loss coefficient
P	wetted or heated perimeter
Q	volumetric rate of flow

List of Figures

Contents

Chapter 1

Introduction

The goal of this report is to describe the methodology and assumptions associated in performing a Best Estimate Analysis with Uncertainty (BEAU) of the critical Large LOCA. The code chosen for the analysis is the Reactor Excursion and Leak Analysis Program(RELAP). Theoretical aspects along with detailed description of the code have been presented in the code manuals. We therefore do not discuss the code here but only refer to some of its characteristics. The basic equation of the code require the conservation of mass, momentum and energy. The considered facility is subdivided into a number of hydrodynamic nodes with connection between the nodes representative of the considered facility. Material properties and correlations have been defined in such a way that the model provides an adequate representation of the facility under steady state and transient conditions. Several versions of the code exist. The particular version of the code used in this report is RELAP5/SCDAP mod 4.0, developed at Idaho National Laboratories, although the model is believed to be compatible with mod 3.3 used by the USNRC. While the code was initially designed for application to LWR transient analysis[26], the code is robust enough to be applied to CANDU reactors[14, 17]. The RELAP code has been extensively validated against experimental data[30] including LLOCA tests at the RD-14, and RD-14M facilities[15, 16]. The cited literature provides a justification in the application of the code in the context of this report. The plant chosen for analysis in this report is a Generic CANDU 900 MW Plant modeled after Darlington NGS.

Chapter 2 provides a definition of the LBLOCA scenario as well as an introduction to the uncertainty methods used in this report.

Chapter 3 provides the modeling methodology used in generation of an input model. A general description of the CANDU 900 MW plant is provided along with calculations of the main components of the HTS. Calculations of uncertainties for each of the considered parameters have been provided alongside their derivations. It is hoped that this approach will provide a more concise and readable presentation. Uncertainties for considered plant parameters are derived from open literature as well as operating data for Darlington NGS unit I and unit IV. Where no source was available, a conservative estimate for the uncertainty was assumed.

Chapter 4 provides transient results as well as uncertainty analysis. A critical break search is implemented for various break sizes between 20% to 100% with net energy deposited in the core used as the chosen figure of merit. A parametric phenomena study is performed discussing the effect of various parameters on governing phenomena. The latter part of the chapter contains a comparison of three methods of analysis; the LOE approach provides a conservative estimate for reactor peak power and bulk net energy deposited chosen as the FOM, the GRS method provides an upper bound for the 95^{th} percentile of the mentioned FOMs, and a brute force Monte-Carlo simulation provides a probability distribution for the mentioned FOMs.

Chapter 5 provides a summary of the performed work as well as recommendations for future analysis.

Chapter 2

Scenario Definition and Literature Review

The Large Break LOCA scenario can be subdivided into various phases characterized by certain behaviors during each phase[?]. The depressurization of the HTS caused by the break results in immediate voiding in the broken loop which is accompanied by a rapid increase in power due to the positive void reactivity feedback. The increase in power is terminated by the activation of the emergency shutdown system. During the Power Pulse Phase of the postulated accident(0-5s following the break), reactor cooling capability is degraded. The large amount of energy is deposited in the fuel results in a rapid increase in fuel temperatures with maximum fuel centerline temperatures occurring within the first 2s of the break. Fuel heat up rate, maximum fuel centerline temperature, the net energy deposited in the core, and the neutron power transient are important characteristics of this stage. HTS blowdown continues during the Early Blowdown Period(5-30s) until the activation of the Emergency Coolant Injection System(ECIS) at around 30s. Maximum Sheath temperatures are reached at around 10-15s following the break. Radiation cooling becomes a significant mode of heat transfer with significant increase in pressure tube temperatures. Cooling of the fuel and pressure tube, fuel integrity, heat load to the moderator, and HTS depressurization rate are of importance during this stage of the transient. The late Blowdown period(30-200s) starts upon the activation of the ECIS. The mass added by the ECIS results in a temporary recovery in the coolant flow and inventory of the broken loop. Naturally, if the break flow is greater than that provided by the ECIS, the HTS inventory continues to decrease as a result of the break.

In mathematical terms, prediction of transient results for a nuclear facility can often be thought of as[22]:

$$\bar{y}(t) = C(t, \bar{x})\bar{x} \tag{2.1}$$

where $\bar{x}, \bar{y}$are input, output variables respectively. In the above equation, C refers to a non linear operator with some dependence on the parameter $\bar{x}$. Once a safety interval is constructed, an input configuration can be defined as safe if the corresponding output lies in the safety interval. Configurations leading to results outside this safety range are deemed as unsafe[22].

According to the USNRC guidelines, limiting conditions for operations are defined in 10CFR50.36 as[22] "the lowest functional capability or performance level of equipment required for safe operation of the facility when a limiting condition for operation of a nuclear reactor is not met, the licensee shall shutdown the reactor or follow any remedial action permitted by the technical specification until the condition can be met". The above statement applies to plant operation under steady state and various hypothesized accident scenarios. Two methodologies used in the prediction of the performance level of the equipment are described below.

Traditionally, the approach in safety analysis has been a conservative one. In the conservative approach, safety is weighted more than in any physical situation. Therefore a situation is chosen that while deemed unrealistic results in rather unfavorable prediction. Therefore, it is safe to assume that any realistic situation will lead to better results. It naturally follows that if the conservative approach predicts that the conservative state is safe, then any real situation can be assumed to be safe. [22] The approach can be implemented by setting key plant parameters at their worst permissible values resulting in the unrealistic system configuration. An unfavorable consequence of this approach is that it may result in predictions of small safety margins which may lead to reductions in operating limits such as reductions in reactor power or to the implementation of design changes.

Best Estimate methods provide an alternative approach. A best estimate for the uncertain parameters results in the most probable system configurations. However, due to occurring deviations in the parameters from their best estimate values, existent measurement errors due to instrument uncertainties, as well as inherent uncertainties in the code/modeling , uncertainties exist in each of the plant parameters. The actual value of a parameter can therefore be thought of as[23]:

$$x_{actual} = x_{\mathrm{be}} + \text{plant uncertainties} + \text{code uncertainties} \tag{2.2}$$

where x_{be} is the best estimate of the considered parameter. The overall effect of these uncertainties of the output parameters can be estimated through an integrated uncertainty analysis. Typically, application of best estimate methods leads to the prediction of higher safety margins. It is required to know the interval(domain) as well as the probability distribution function for each of the considered input parameters. These may be found from various literature sources, calculations for instrument uncertainties, and plant operating data. Sensitivity analysis may be performed to identify latent parameters ie. parameters whose uncertainties need not be analyzed. Using proper sampling of the input parameters, Monte Carlo methods may be used to predict the distribution function for the output variables.

Direct Monte-Carlo methods are fairly straightforward[46]. The input sample distribution can be sampled n times, and the code may be run directly to generate n outputs. The acquired outputs can be used to generate an actual distribution. The method typically requires a high number of runs, requiring large computation time for large nodalization schemes. Response surface functions provide an alternative approach[46]. The code is run with specific input variables to generate a number of outputs. A polynomial fit is performed from the data points to generate a response surface. The response surface is then treated as a surrogate of the code, to which a Monte Carlo simulation is applied to generate the output probability function distribution[47]. Reference [45] provides the methodology as well as results for the application of FSR methods to a postulated LBLOCA of Pickering B station using the TUF thermal hydraulics code. The report successfully demonstrates that[45] "that the consequences of a hypothetical LBLOCA are significantly more benign than analysis performed using LOE assumptions" when using Best Estimate methods. GRS methods, based on non parametric statistics and use of Wilk's formula, provide an alternative method for predicting the statistical tolerance of the output without the need of a probability function distribution. A number of n code runs are performed in which all uncertain parameters are varied simultaneously to generate n outputs. The n values of the output are sorted such that [48] $Y(1) \leq Y(2)...Y(n-1) \leq Y(n)$. From the application of Wilk's formula [48, 13], $Y(n)$ provides an upper bound for the $a * 100$ percentile of the output distribution with the $b * 100$ confidence level with a, b, and n related as[13]:

$$1 - a^n \geq b \tag{2.3}$$

In practice, the 95% confidence limit of the 95^{th} percentile is recommended by the USNRC[46]. The number of runs n required for a 95^{th} percentile with a 95% confidence level for the one-sided tolerance limit is provided as 59 runs. Glaeser[48] concludes that the method may be used successful to predict a 95/95 upper bound of peak clad temperatures for a simulated LBLOCA (2*100% cold leg break) of a 1300 MW electric power German PWR reactor.

Chapter 3

Modeling and Methodology

3.1 Overall Plant Description

The design of the CANDU 900 MW plant is essentially the same as that of Darlington NGS. The reactor core is enclosed by a horizontally placed cylindrical tank called the Calandria, which is filled with the heavy water moderator. It is pierced by 480 calandria tubes positioned along its axial length. The calandria tubes are arranged on a 285.75 mm square pitch forming a circular lattice array[19]. Each calandria tube has within it a smaller a pressure tube/fuel channel, with the annulus between the two tubes filled with CO_2 gas. This provides thermal isolation between the pressure tubes and the comparatively cool moderator. Each pressure tube is connected to an end-fitting made primarily of stainless steel. Within each pressure tube are twelve or thirteen fuel fuel bundles. Each bundle contains a total of 37 fuel rods arranged in four circular rings. The table below describes the calandria tubes, fuel channels, and fuel rods[19].

Fuel Pellet outside diameter(average)	12.15 mm
Cooolant corss sectional flow area	34.19 cm^2

Pressure tube material	Zr-Nb
Pressure tube inner radius	51.7 mm
Pressure tube outer radius	55.9 mm
Calandria tube material	Zircaloy 2
Calandria tube inner radius	64.5 mm
Calandria tube oter radius	65.9 mm
Reactor length(Calandria tube sheet to Clandria tube sheet)	5.944 m

Pressurized heavy water circulating in the primary heat transport system (PHTS) provides cooling to the reactor fuel rods which lie inside the pressure tube, thereby removing the heat produced by the fission of the natural uranium fuel. The primary heat transport system is comprised of two loops (north and south). Each loop contains two core passes(east and west) and supplies coolant to 240 (half of the core) channels. The passes have opposite flow directions so that flow in adjacent channels is in opposing directions.

Each loop contains two reactor inlet headers, two reactor outlet headers, two steam generators, and two pumps. Coolant flows to the core through the 480 inlet feeder pipes connecting the inlet headers to the inlet end-fittings, and flows out of the core from the outlet end-fittings to the reactor outlet headers through a corresponding number of outlet feeders. Reactor outlet headers from the north loop and south loop are connected through two balance lines. Each outlet header is connected to the corresponding steam generator inlet. The removed heat from the core is transferred to the natural water flowing in the steam generator to form steam which subsequently drives the turbine generator. Heat transport pumps provide forced convective flow by acting as pressure sources.

PHTS pressure and inventory are controlled through a pressure and inventory circuit and control program, the details of which will be discussed later. Reactor power is measured from 23 vertical, and 14 horizontal in-core flux detectors. Six ion chambers assemblies installed in the reactor provide the reactor log power. Reactivity is controlled through adjuster and absorber rods, using power measurements as the deriving parameter. Two shutdown systems(SDS1 and SDS2) may provide rapid termination of reactor operation in case of a power excursion.

3.2 System Representation

The above system has been modeled in RELAP5. The model consists of three major parts: heat transport, pressure and inventory control, and secondary side. The modeling strategy and calculations for each of these three systems are discussed below. With the exception of the channels, end-fittings, and certain components of the steam generator, all hydrodynamic components are assumed to be comprised of carbon steel and have an internal wall roughness of $\epsilon = 45.72 * 10^{-6}$ m. Heat transfer through piping walls is accounted for in all of the heat transport and secondary side systems. The heat transfer areas are calculated based on the inside (wetted) dimensions of the components, and the mass of the piping.

In selecting a nodalization for the hydrodynamic components, the guidelines in reference [27] have been followed. In particular, volume lengths have been chosen in such a way that all components have similar material Courant limits(volume length divided by fluid velocity), and all volumes have a length to diameter ratio of greater than unity.

3.2.1 Headers

A schematic of the inlet header is shown in figure 4.5.

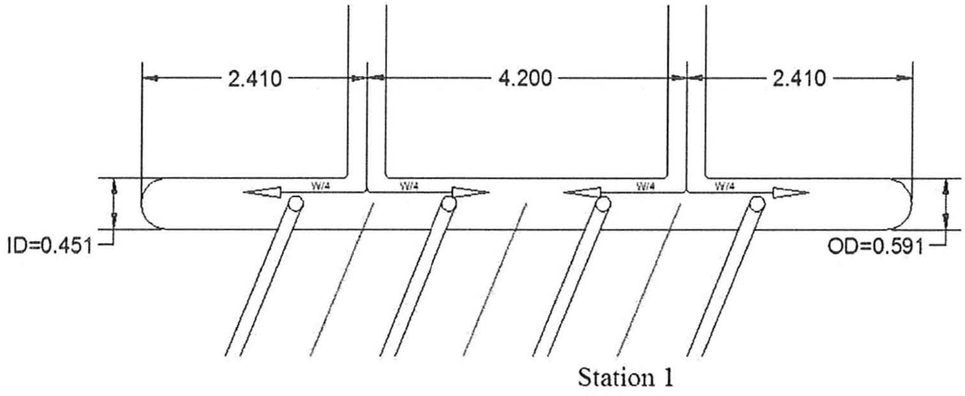

Figure 3.1: Schematic of the Inlet Header

Coolant discharged from either of the two pump legs enters the reactor inlet header at a design pressure of 11.3 MPa[20] and splits amongst the 120 inlet feeders. As the feeders are of different sizes and connect to the reactor header at different locations(polar, axial, and radial), it is quite cumbersome to come up with an entrance loss coefficient for each feeder. Instead a loss coefficient for the average feeder is calculated. It is assumed that the flow splits evenly in the header and then evenly amongst six groups of feeders. It follows that:

Average flow in the header	W/4
Average flow into the inlet feeder	W/120
Average area of the inlet feeder(reference [9])	0.0027 m^2
Area of the header(reference [8])	0.1598 m^2

The effective liquid velocity of approach V_p along the header is shown in the figure 3.2[18].

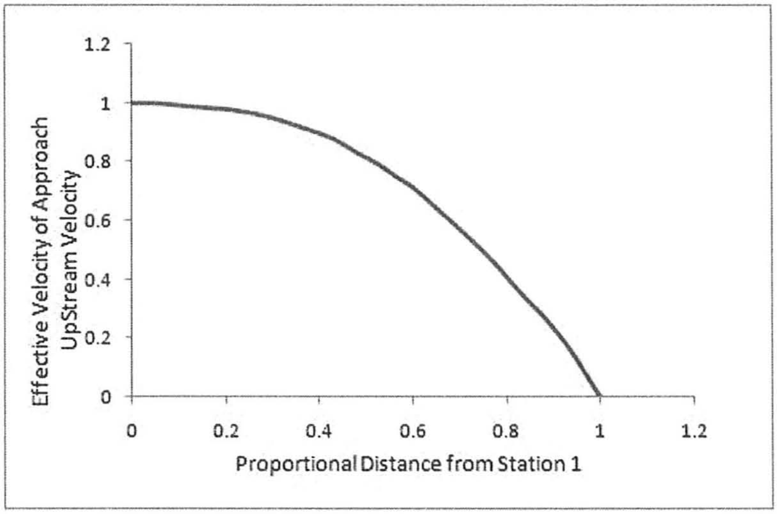

Figure 3.2: Effective velocity of approach into the feeder relative to upstream velocities

For the velocity in the average feeder position, the approach velocity is given as 0.8. The velocity ratio is then found to be:

$$\frac{V_p}{V_3} = \frac{\frac{W/120}{0.324101}}{\frac{0.8W/4}{0.1598}} = 2.2 \tag{3.4}$$

From page 456 of Idlechik, for a square edged tee with $\frac{F_s}{F_{st}} = 1$, the minor loss is equal to $K_{inlent} = 1.8$ Pa/Pa. A similar calculation for the outlet header incase of flow reversal is found to be $K_{outlet} = 1.5$ Pa/Pa. The feeder-header connections being smooth, the loss is expected to be somewhat less than the reported. Losses from feeders into the headers are reported as 0 Pa/Pa in reference [18].

3.2.2 Core Modeling

Feeder geometries for the 240 channels in the north loop can be found in reference[9]. A RELAP5 input model for each channel was constructed using appropriate minor losses for each feeder. Losses through elbows were calculated from[18]:

$$K = k_{\Delta} k_{Re} A_1 B_1 + 0.0175 f \frac{R_c}{D_h} \delta^{\circ} \tag{3.5}$$

where:

$$\begin{aligned}
k_{\Delta} &= 1 + \epsilon^2(10^6) && \text{for } R_e \geq 4 * 10^4 \\
k_{Re} &= 1.0 && \text{for } R_e \geq 4 * 10^4 \\
A_1 &= 0.9 \sin \delta^{\circ} && \text{for } \delta^{\circ} \leq 70^{\circ} \\
&= 1.0 && \text{for } \delta = 90^{\circ} \\
&= 0.7 + 0.35 \tfrac{\delta^{\circ}}{90} && \text{for } \delta^{\circ} \geq 100^{\circ} \\
&= 0.8457 + 0.007715(\delta^{\circ} - 70^{\circ}) && \text{for } 90 > \delta^{\circ} > 70^{\circ} \\
&= 1.0 + 0.008889(\delta^{\circ} - 90^{\circ}) && \text{for } 100 > \delta^{\circ} > 90^{\circ} \\
B_1 &= 0.21/\sqrt{R_c/D_h}
\end{aligned}$$

The hydraulic diameter D_h, the bend radius of curvature R_c, and the bend angle δ° were provided for each bend in reference [9]. The friction factor f was calculated from the colebrook equation using a roughness of $\epsilon = 45.72 * 10^{-6}$m. Losses through reducers and diffusers were calculated in terms of the larger cross sectional are as follows[40]:

$$\begin{aligned}
&\text{contraction} && K = \tfrac{0.8 \sin \frac{\theta}{2}(1-\beta^2)}{\beta^4} \\
&\text{expansion} && K = \tfrac{2.6 \sin \frac{\theta}{2}(1-\beta^2)^2}{\beta^4}
\end{aligned}$$

where $\beta = \frac{D_1}{D_2}$ is the ratio of the smaller pipe diameter D_1 to the larger pipe diameter D_2 and θ is the angle over which the reduction takes place and is provided in [9] for each feeder.

Losses for orifices were calculated as $K = \frac{C}{\sqrt{1-\beta^4}}$ where C is the discharge coefficient calculated from $C = 0.5959 + 0.0312\beta^{2.1} - 0.184\beta^8 + \frac{91.71\beta^{2.5}}{Re^{0.71}}$[37] and $\beta = \frac{D_t}{D_0}$ is the ratio of the orifice throat diameter to the pipe diameter provided for each feeder in [9].

Comparisons with plant operation data for the 22 finch channels in the west loop are shown in figure4.5.

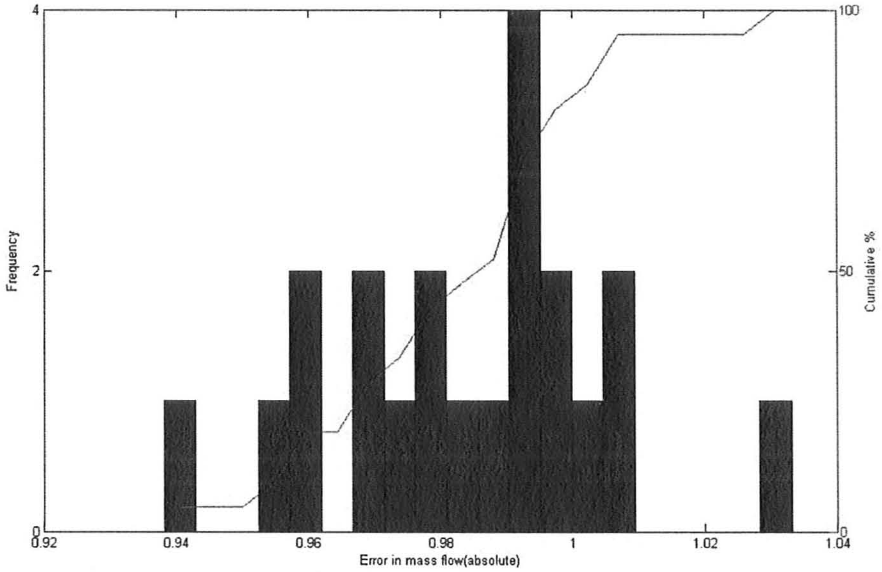

Figure 3.3: Error distribution for mass flows

The error ϵ for the flows is a function of the RELAP5 predicted mass flow $\dot{m}_{theoretical}$ and the measured mass flow $\dot{m}_{exp}$ as follows: $\epsilon = 1 - \frac{\dot{m}_{theoretical} - \dot{m}_{exp}}{\dot{m}_{theoretical}}$. Analysis of the error histogram shows the data to be an unbiased normal with a standard deviation of $\sigma = 0.0218$. The corresponding uncertainty in pressure losses can be calculated as follows: from the Bernoulli equation, the mass flow $\dot{m}$ can be related to the minor loss K by $\Delta P - g\Delta z = \frac{1}{2}(K + \frac{fL}{D})\frac{\dot{m}^2}{\rho A^2}$. Let $c = K + \frac{fL}{D}$. Assuming that the pressure drop and the elevation are perfectly known, we then have:

$$|\frac{\delta c}{c}| = 2\frac{\delta \dot{m}}{\dot{m}} \tag{3.6}$$

The uncertainty on K and f can therefore be taken as $\sigma = 2 * 0.0218 = 0.0436$. Since no multiplier for f is available in RELAP5, the corresponding uncertainty on the relative roughness $\frac{\epsilon}{D}$ must be calculated for input. The turbulent friction factor f is calculated in RELAP5 from the Zigrang-Sylvester aproximation[29]. The correlation has the form:

$$\frac{1}{\sqrt{f}} = -2.0\log(\frac{\epsilon}{d}\frac{1}{3.7} - 5.02\frac{A}{Re}) \tag{3.7}$$

where $A = \log(\frac{\epsilon}{D}\frac{1}{3.7} - (\frac{5.02}{Re}\log(\frac{\epsilon}{D}\frac{1}{3.7} + \frac{13}{Re}))$. The correlation is valid for $4000 \leq Re$ and $0.00004 \leq \frac{\epsilon}{D} \leq 0.05$. Comparison of the correlation with the colebrook equation shows the difference to be less than the experimental measurement error[29]. It is therefore assumed that the two models can be interchanged without any loss of accuracy. Relative piping roughnesses in the CANDU9 heat transport system vary from 0.001 to 0.006. The turbulent friction flow factor for this range of relative roughnesses lies between 0.01 and 0.04[37]. The uncertainty of the relative roughness is found to be a normal with standard deviations shown in table 3.6. These uncertainties were calculated by first modeling f as an unbiased normal with a standard deviation of 0.0436, then sampling 100000 points via monte-carlo simulation. The relative roughness was then calculated via the colebrook equation for each generated distribution set.

f	$\frac{\epsilon}{D}$	σ for $\frac{\epsilon}{D}$
0.01	$3.7030 * 10^{-5}$	26 %
0.02	0.0011	18 %

0.03	0.0048	15 %
0.04	0.0118	13 %

Table 3.6: Assumed uncertainty for relative roughnesses

Series and parallel averaging methods can be used to represent several feeders as an equivalent pipe with average thermal-hydraulic properties. A single feeder with n cross sectional areas may be averaged into an equivalent pipe with a uniform cross sectional area using the series method. Assume that:

$V = \sum_{i=1}^{n} V_i = \sum_{i=1}^{n} A_i L_i$
$L = \sum_{i=1}^{n} L_i$
$A = V/L$

To conserve the pressure drop between two points:

$$\Delta P = (f\frac{L}{D} + K)\frac{\dot{m}^2}{2\rho A^2} = \sum_i (f_i \frac{L_i}{D_i} + K_i)\frac{\dot{m}^2}{2\rho A_i^2} \tag{3.8}$$

D and K may then be calculated from:

$$\frac{1}{D} = \sum_{i=1}^{n} \frac{f_i}{f}(\frac{A}{A_i})^2 \frac{L_i}{L} \tag{3.9}$$

$$K = \Delta P(\frac{2\rho A^2}{\dot{m}^2}) - f\frac{L}{D} \tag{3.10}$$

Where ΔP refers to the difference in pressures between the inlet/outlet header and the endfitting inlet/outlet. A similar procedure can be used to average n feeder pipes into a single pipe using the parallel averaging scheme. Assume that:

$V = \sum_{i}^{n} V_i = \sum_{i=1}^{n} A_i L_i$

$L = \frac{1}{n}\sum_{i=1}^{n} L_i$

$A = V/L$

$\dot{m} = \sum_{i=1}^{n} \dot{m}_i$

$\Delta z = \frac{1}{n}\sum_{i=1}^{n} \Delta z_i$

If equivalent hydraulic diameter is defined as:

$$\frac{1}{D} = \frac{1}{n}\sum_{i=1}^{n} \frac{f_i}{f}\frac{1}{D_i}\frac{L_i}{L}\left(\frac{A/n}{A_i}\right)^2 \tag{3.11}$$

then the equivalent minor loss can be found from equation 3.10 with $\rho = \frac{\sum_i^n \dot{m}_i \rho_i}{\dot{m}}$.

Figure 3.4 shows the channel grouping scheme for the 240 channels in the CANDU 900 core loop. The first number in each cell of the the figure is the best estimate for channel power (kW) reported in reference [9] and the second is the the channel mass flow(kg/s) calculated by RELAP5. Channels without shading are located in the broken pass. The basic model used in reference [20] represents each core by-pass as 120 identical channels with average characteristics. A more detailed model has also been implemented, which uses six separate core regions per by-pass(in the broken loop), with each region representing channels having similar thermal hydraulic conditions. In selection of channel groupings effects of elevation, channel power, flow, as well as feeder volumes and areas have been considered. Regions 1 and 6 contain channels with low flows and powers located at the outer perimeter of the core. Most of the inlet feeders in this region have an orifice placed in the first horizontal run following the header to reduce the flow. Feeders in this region also have smaller cross sectional areas. Regions 2, and 5 are channels with high flows and intermediate to high channel powers. Regions 3 and 4 represent channels with high flows and high powers. In addition to the six region representation, the channel with the highest power (channel O9) is modeled separately and used in the BE, and NED calculations.

The effect of channel grouping on the HTS response is examined in chapter 4.

A detailed channel model using a 24 nodes has been modeled. Fuel channel models using 6 and 12 nodes have also been implemented and a sensitivity study on the effect of nodalization is performed in chapter 4. The frictional loss coefficient for 12 bundles is reported as 9.7944 Pa/Pa in reference [18]. This loss is assumed to occur at each bundle. Effects of channel creep, and alignment of bundles contribute to the total pressure drop. Axial and radial creep is not modeled. The effect of bundle misalignment is addressed by considering the uncertainty on the minor pressure drop to have the form of a uniform/rectangular distribution with a width of ±10%.

The initial normalized axial power distribution of the channel is assumed to be a sinusoidal curve with no flux tilt. The relative axial power p_i for node i is calculated as $p_i = \int_{L_i}^{L_i+1} \sin(\frac{\pi x}{L})dx$ where L_i and L_{i+1} are the lengths at the start and end of the node respectively. The 37 fuel elements are modeled using four heat structures representing the center, inner, intermediate, and outer rings with the wetted perimeter defined as $n * P_w$ where n is the number of fuel pins in each ring and $P_w = 0.01308\pi = 0.04108\text{m}$ is the wetted perimeter corresponding to a single pin. The radial heat flux distribution in terms of relative axial power is given in the table below.

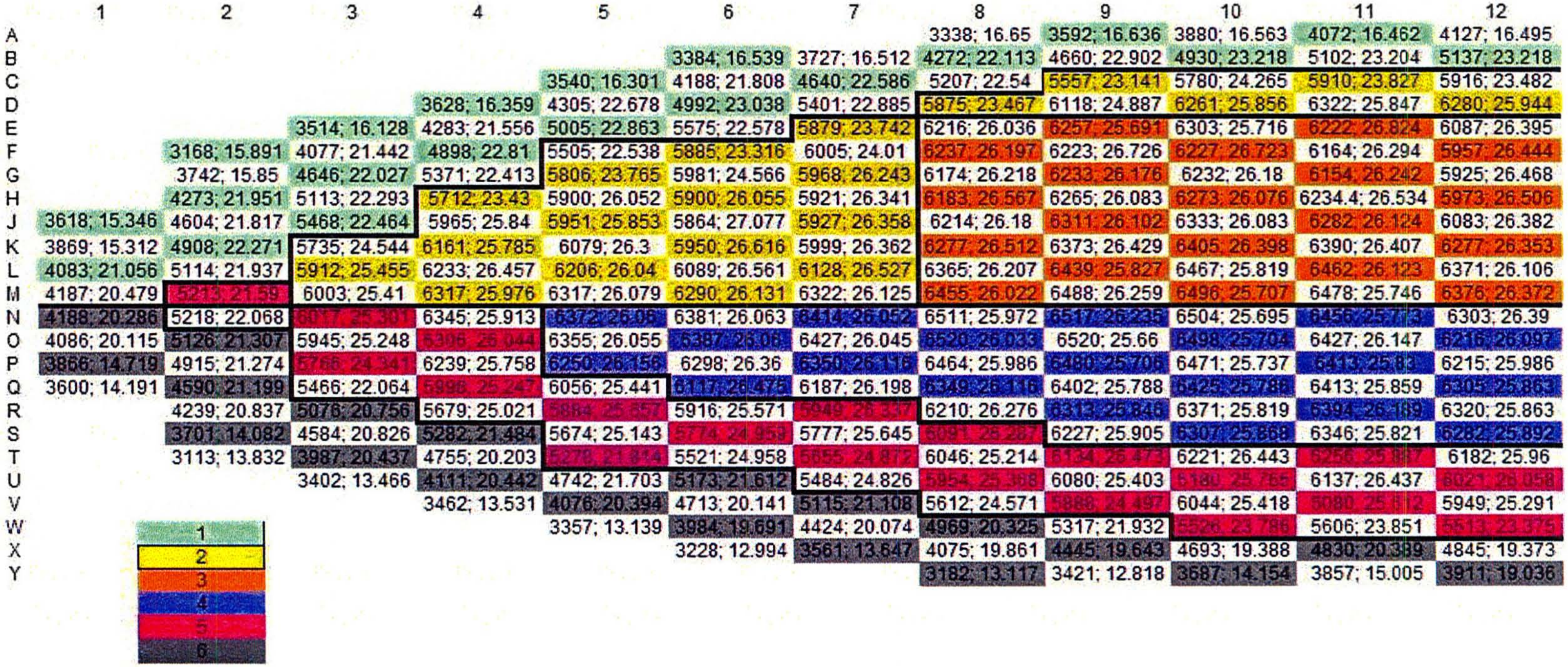

	1	2	3	4	5	6	7	8	9	10	11	12
A								3338; 16.65	3592; 16.636	3880; 16.563	4072; 16.462	4127; 16.495
B						3384; 16.539	3727; 16.512	4272; 22.113	4660; 22.902	4930; 23.218	5102; 23.204	5137; 23.218
C					3540; 16.301	4188; 21.808	4640; 22.586	5207; 22.54	5557; 23.141	5780; 24.265	5910; 23.827	5916; 23.482
D				3628; 16.359	4305; 22.678	4992; 23.038	5401; 22.885	5875; 23.467	6118; 24.887	6261; 25.856	6322; 25.847	6280; 25.944
E			3514; 16.128	4283; 21.556	5005; 22.863	5575; 22.578	5879; 23.742	6216; 26.036	6257; 25.691	6303; 25.716	6222; 26.824	6087; 26.395
F		3168; 15.891	4077; 21.442	4898; 22.81	5505; 22.538	5885; 23.316	6005; 24.01	6237; 26.197	6223; 26.726	6227; 26.723	6164; 26.294	5957; 26.444
G		3742; 15.85	4646; 22.027	5371; 22.413	5806; 23.765	5981; 24.566	5968; 26.243	6174; 26.218	6233; 26.176	6232; 26.18	6154; 26.242	5925; 26.468
H		4273; 21.951	5113; 22.293	5712; 23.43	5900; 26.052	5900; 26.055	5921; 26.341	6183; 26.567	6265; 26.083	6273; 26.076	6234.4; 26.534	5973; 26.506
J	3618; 15.346	4604; 21.817	5468; 22.464	5965; 25.84	5951; 25.853	5864; 27.077	5927; 26.358	6214; 26.18	6311; 26.102	6333; 26.083	6282; 26.124	6083; 26.382
K	3869; 15.312	4908; 22.271	5735; 24.544	6161; 25.785	6079; 26.3	5950; 26.616	5999; 26.362	6277; 26.512	6373; 26.429	6405; 26.398	6390; 26.407	6277; 26.353
L	4083; 21.056	5114; 21.937	5912; 25.455	6233; 26.457	6206; 26.04	6089; 26.561	6128; 26.527	6365; 26.207	6439; 25.827	6467; 25.819	6462; 26.123	6371; 26.106
M	4187; 20.479	5213; 21.59	6003; 25.41	6317; 25.976	6317; 26.079	6290; 26.131	6322; 26.125	6455; 26.022	6488; 26.259	6496; 25.707	6478; 25.746	6376; 26.372
N	4188; 20.286	5218; 22.068	6017; 25.301	6345; 25.913	6372; 26.06	6381; 26.063	6414; 26.052	6511; 25.972	6517; 26.235	6504; 25.695	6456; 25.713	6303; 26.39
O	4086; 20.115	5126; 21.307	5945; 25.248	6306; 26.044	6355; 26.055	6387; 26.06	6427; 26.045	6520; 26.033	6520; 25.66	6498; 25.704	6427; 26.147	6216; 26.097
P	3866; 14.719	4915; 21.274	5766; 24.341	6239; 25.758	6250; 26.156	6298; 26.36	6350; 26.116	6464; 25.986	6480; 25.706	6471; 25.737	6413; 25.83	6215; 25.986
Q	3600; 14.191	4590; 21.199	5466; 22.064	5998; 25.247	6056; 25.441	6117; 26.475	6187; 26.198	6349; 26.116	6402; 25.788	6425; 25.788	6413; 25.859	6305; 25.863
R		4239; 20.837	5076; 20.756	5679; 25.021	5884; 25.557	5916; 25.571	5949; 26.337	6210; 26.276	6313; 25.846	6371; 25.819	6394; 26.189	6320; 25.863
S		3701; 14.082	4584; 20.826	5282; 21.484	5674; 25.143	5774; 24.959	5777; 25.645	6091; 26.287	6227; 25.905	6307; 25.868	6346; 25.821	6282; 25.892
T		3113; 13.832	3987; 20.437	4755; 20.203	5278; 21.814	5521; 24.958	5655; 24.872	6046; 25.214	6134; 25.473	6221; 26.443	6256; 25.887	6182; 25.96
U			3402; 13.466	4111; 20.442	4742; 21.703	5173; 21.612	5484; 24.826	5954; 25.368	6080; 25.403	6180; 25.765	6137; 26.437	6021; 26.058
V				3462; 13.531	4076; 20.394	4713; 20.141	5115; 21.108	5612; 24.571	5888; 24.497	6044; 25.418	6080; 25.612	5949; 25.291
W					3357; 13.139	3984; 19.691	4424; 20.074	4969; 20.325	5317; 21.932	5526; 23.786	5606; 23.851	5513; 23.375
X						3228; 12.994	3561; 13.647	4075; 19.861	4445; 19.643	4693; 19.388	4830; 20.389	4845; 19.373
Y								3182; 13.117	3421; 12.818	3687; 14.154	3857; 15.005	3911; 19.036

1
2
3
4
5
6

Figure 3.4: Channel grouping scheme

Element Ring	# of fuel pins	% of node axial power
center	1	22 %
inner	6	23 %
interm	12	25 %
outer	18	30 %
total	37	100 %

Temperature dependent material properties for the uranium dioxide fuel have been taken from the MATPRO libraries. For the UO_2 specific heat, reference [31] quotes an accuracy of ±3% for fitting the data of Kerrisk and Clifton over a temperature range of 300 to 3000 K, with an approximately uniform distribution relative to temperature(i.e temperature independent). Therefore, the uncertainty for the specific heat data is taken to be an unbiased normal with a standard deviation of 3%. For the temperature dependent thermal conductivity, reference [31] suggests that the data of Bates is

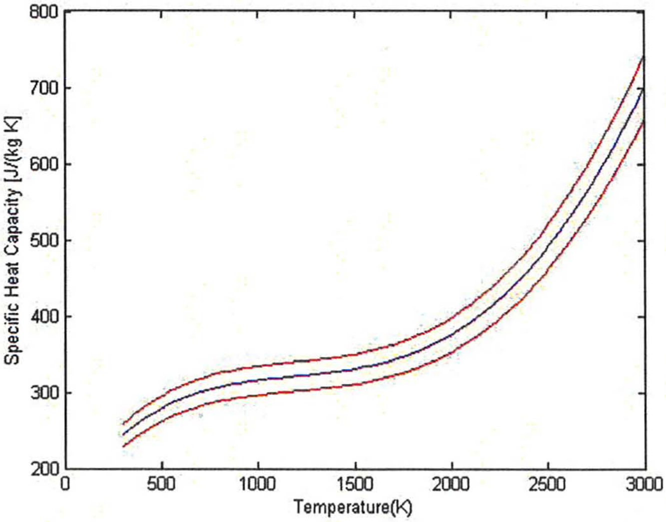

Figure 3.5: Specific heat capacity of UO_2 with $\pm 2\sigma$

applicable for densities greater than 96% of the theoretical density. For input, the thermal conductivity from Bates measurement of thermal diffusivity $\alpha = \frac{k}{C_p \rho}$, where C_p is the specific heat at constant pressure, ρ is the density of the UO_2 sample, and k is the thermal conductivity is fitted against a sixth order polynomial. The error distribution is found to follow an unbiased normal with a standard deviation of $\sigma = 3.81\%$. The experimental measurement error of the data is reported at 2%. Therefore, the uncertainty for the fuel thermal conductivity is taken to follow a standard normal with a standard deviation of $\sigma = 4.3\%$.

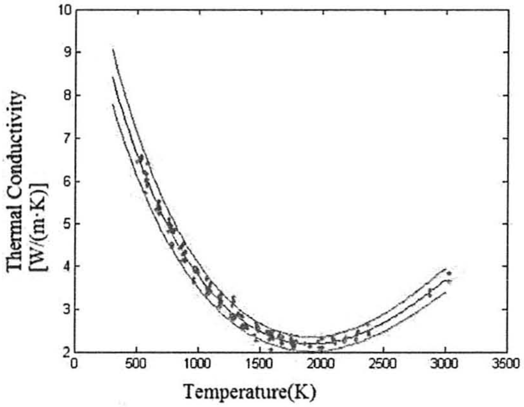

Figure 3.6: Model prediction for thermal conductivity of UO2 compared to data from Bates

Inlet and outlet end-fittings are modeled as a single volume with equivalent hydraulic properties . Minor loss coefficients are reported in the table below [18]. The flow path through the end-fitting can be divided into three sections: an annular flow path between the endfitting inner diameter and the outer perimeter of the liner tube, a flow area providing passage from this annular space into the channel, and a stagnant D_2O volume behind the endfitting shield plug. Unfortunately, no available data with detailed CANDU endfitting dimensions was found. Therefore, to investigate the effect of endfitting nodalization on the overall HTS response, a three node model of the endfitting was implemented with the volumes and flow paths for each of these

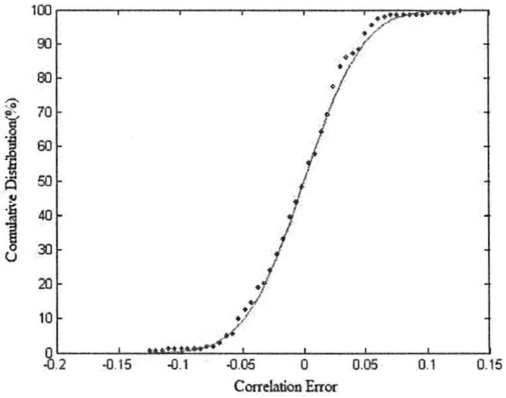

Figure 3.7: Cumulative Distribution of the error= $\frac{k_{correlation}-k_{experimental}}{k_{experimental}}$

sections estimated from figure 11.5 of reference [38].

Inlet End-fitting	3.033 Pa/Pa
Outlet End-fitting	3.454 Pa/Pa

Table 3.10: Values of loss coefficient K for 37-Element Fuel Bundles

3.2.3 HTS Pumps

The primary heat transport system contains four pumps which provide forced convective flow of coolant under normal operating conditions. Under transient conditions, reactor cooling capability must be maintained in order to keep fuel sheath temperatures from exceeding the specified safety limits. In the case of a LLOCA, the rapid depressurization of the primary heat transport circuit results in the coolant reaching saturation conditions and the occurrence of flashing at the throttling point either inside the pump or elsewhere in the loop. This leads to a two phase fluid flow through the circuit. The response of the pump under these two phase conditions differs significantly from that of the single phase region and is modeled through empirical head multipliers obtained from steady state experimental data.

The pump component in RELAP5 is volume oriented and the pump head H is modeled as providing an additional body force equal to $\rho g H$ which is added to the mixture momentum equation with a leading coefficient of $\frac{1}{2}$. The pump head H^{n+1} at the new time step is calculated from:

$$H^{n+1} = H^n + (\frac{dH}{dQ})^n (Q^{n+1} - Q^n) \tag{3.12}$$

The values of the pump head and its derivative are calculated from lookup tables. The regions of operation within the pump can be grouped based on the direction of flow and rotation:

1st quadrant:	forward flow and forward rotation (normal pumping quadrant)
2nd quadrant:	reversed flow and forward rotation (dissipation quadrant)
3rd quadrant:	reversed flow and reversed rotation (normal turbine quadrant)
4th quadrant:	forward flow and reversed rotation (reverse quadrant)

In the case where a rupture occurs near the pump intake, for a short period following the rupture, the pump impeller will continue to rotate forward while coolant direction is reversed. The second quadrant of the graph characterizes this mode of operation. If the rupture occurs near the pump outlet, coolant will begin to force itself through the pump and the pump will operate in the the dissipative and turbine region of the first quadrant[10].

The CANDU 900 is equipped with four identical primary heat transport pumps. Pump Properties are listed in the table below[20]:

Variable	Value
Normal Pump Operation Speed	188 radians/s
Reference Head	221m
Reference Flow per pump	3.3 m^3/s
Ratio of torque to inertial	23 $1/s^2$
Reference Density	872 kg/m^3

Head-flow characteristics are defined through dimensionless homologous curves relating the dimensionless head ratio $y = h/a^2$ or $y = h/v^2$ as a function of homologous values of $x = a/v$ or $x = v/a$ where h is defined as the ratio of the actual head H to the rated head H_R, a is the ratio of the measured speed N to the reference speed N_R and v is the ratio of the volumetric flow Q to the rated flow Q_R. Single phase pump data is presented in the figure below.

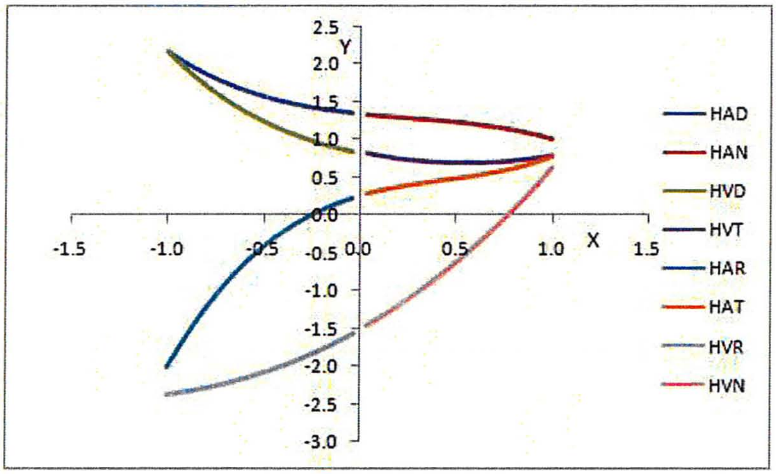

Figure 3.8: Single Phase Pump Characteristics

The abbreviations are used in designating the characteristic pump curves in various quadrants of operation. H represents the head ratio, V designates that homologous characteristic ratio h/v^2 is provided against v/a while A is the case where the ratio h/a^2 is provided against a/v. The last letter of the three digit symbol represents the operation quadrant of the pump: N represents normal operation, D represents energy dissipation and T represents the turbine operation region and R corresponds to the case in which the pump impeller is rotating in reverse of its intended direction[11]. Table 3.13 below summarizes the regions described by each curve[7].

Quadrant	Symbol	Values	Flow	Head
1st	HAN	$Q > 0, H > 0, N > 0, a > 0, v > 0, v/a < 0$	v/a	h/a^2
	HVN	$Q > 0, H > 0$ or $H < 0, N > 0, a > 0, v > 0, v/a > 0$	a/v	h/v^2
2nd	HAD	$Q < 0, H > 0, N > 0, a > 0, v < 0, v/a > -1.0$	v/a	h/a^2
	HVD	$Q < 0, H > 0, N > 0, a > 0, v < 0, v/a < -1.0$	a/v	h/v^2
3rd	HAT	$Q < 0, H > 0, N < 0, a < 0, v < 0, v/a < 1.0$	v/a	h/a^2
	HVT	$Q < 0, H > 0, N < 0, a < 0, v < 0, v/a < 1.0$	a/v	h/v^2

4^{th}	HAR	$Q > 0, H > 0$ or $H < 0, N > 0, a < 0, v > 0, v/a > -1.0$	v/a	h/a^2
	HVR	$Q > 0, H < 0, N > 0, a < 0, v > 0, v/a < -1.0$	a/v	h/v^2

Table 3.13: Regions of pump operation

The gained head in pumps is considerably degraded under two phase flow conditions. RELAP5 calculates the degraded head under two phase conditions as a product of a head multiplier $M(\alpha)$ and the difference $\Delta h_{1\phi-2\phi}$ between the single phase head $h_{1\phi}$ and a two phase fully degraded head curve $h_{2\phi}$. The pump head is calculated from[26]:

$$h = h_{1\phi} - M(\alpha)\Delta h_{1\phi-2\phi} \tag{3.13}$$

The CANDU 900 pump is modeled in SOPHT using the Aerojet Nuclear Company(ANC) two phase correlation models for the head difference and the difference curve multiplier[12]. To maintain consistency, the same model is used in the RELAP5 input. The ANC two-phase correlations are based upon four distinct sets of performance data under: steady state single phase subcooled water conditions, steady state two phase steam-water conditions, and transient two phase conditions during a simulated LOCA in the 1-1/2 loop semi scale system. The same pump was used in all four experiments. The table below describes test details[10]:

Pump Description:	
Impeller diameter	197 mm
Impeller Speed	138.9 rev $m^{3/4}/min^{3/2}$
Pump rated head	58.52 m
Pump rated flow	0.011358 m^3
Single Phase Test Conditions:	

Pressure range	0-1.378 Mpa
Temperature	23.9 to 51.7 °C
Flow rate	-200 to 200 % rated flow
Impeller Speed	-100 to 100 % rated speed
Two phase Test Conditions:	
Pressure Range	1.38 to 6.21 MPa
Temperature	190 o 290 °C
Flow rate	-200 to 200 % rated flow
Impeller Speed	-100 to 100 % rated speed
Void fraction	0 to 100 %

The steady state tests were performed at the Atomic Division Laboratory of Westinghouse Canada (WCL) in Hamilton, Ontario. Transient LOCA simulations were performed at the ANC facilities in Idaho with a similar system configuration to the steady state tests. The original ANC head difference data [10] along with the SOPHT values are shown in figure 3.2.3. The SOPHT code calculates the head difference from either of two curves depending on the pump state of operation. For the HAN, HAD, HAT, and HAR regions, the 'within range' head difference curve is used[1] while for the HVN, HVD, HVT, and HVR regions the 'without range' head difference curve is used[2]. While the SOPHT head difference model overlaps with the ANC data in the HAN, and HVN regions, there is notable discrepancy in the other four quadrants of operation. Therefore, both models of head difference have been implemented in RELAP5 and the sensitivity of transient results to the head difference correlations will be analyzed in chapter 4.

It is shown in reference [10] (pg. 3-16) that the head loss ratio $M(\alpha) = \frac{h_{1\phi}-h}{h_{1\phi}-h_{2\phi}}$ is

---

[1] Reference [21], subroutine pump.f lines 88-90

[2] Reference [21], subroutine pump.f lines 93-95

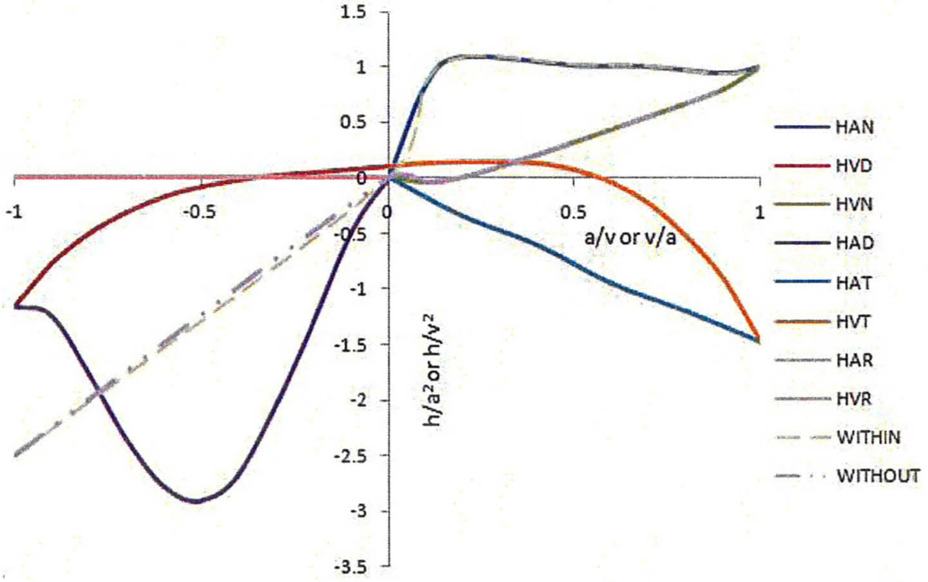

Figure 3.9: Comparison between the SOPHT(within and without) and ANC degraded head difference(HAN, HVD, HVN, HAD, HAT, HVT, HAR, HVR)

essentially a function of the void fraction. For inlet void fractions less than 20 percent, the two phase flow is in the form of dispersed vapor bubbles through a continuous liquid phase. Within this region, "the presence of dispersed bubbles might change the incidence angle or hydraulic response of the pump, and might sometimes give a better performance than for single phase"[7]. At void fractions between 20 to 80 percent, a change in the flow regime from bubbly to slug flow is expected resulting in a larger difference between the single phase head and the actual head. At higher void fractions the flow regime changes to annular/mist, returning to single phase vapor at 100 percent void. It was found in [10] that "the more homogeneous the flow regime the closely the relative losses approach the single phase values", which results in a head multiplier close to 0.

The effect of flow regime on the effective pump head can be captured through the multiplier $M(\alpha)$ in equation 3.13. Three multipliers have been developed by ANC, differing through the value of h used to obtain the multiplier. The Semi-Scale test

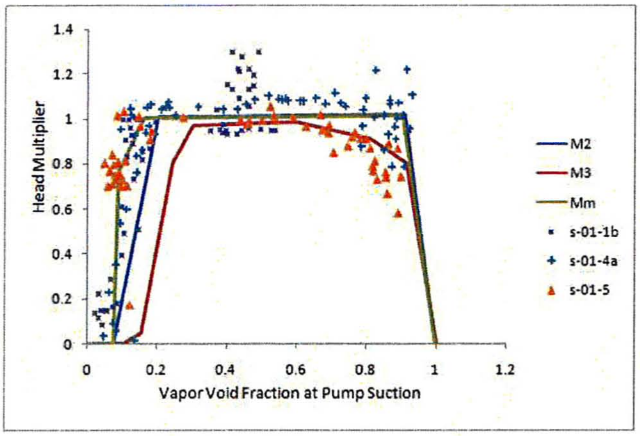

Figure 3.10: Comparison between $M_2(\alpha)$, $M_3(\alpha)$, $M_m(\alpha)$

results along with the multiplier correlations are shown in the figure below. The multiplier $M_2(\alpha) = \frac{h_{1\phi}-h_{ss}}{h_{1\phi}-h_{2\phi}}$ is based on the steady state two phase tests (test no. 1008, 1010) performed at the Westinghouse Canada test loop where h_{ss} is the two phase homologous value measured from the steady state tests. $M_2(\alpha)$ indicates that the two phase head does not change for inlet void fractions of 0 to 8% and increases to a fully degraded value at an inlet void fraction of 20%, staying at this fully degraded value for void fractions lower than 90% and reducing thereon to the head corresponding to the single phase vapor values at a void fraction of 1.0. $M_3(\alpha) = \frac{h_{1\phi}-h_{tr}}{h_{1\phi}-h}$ is calculated from the homologous value h_{tr} of transient two phase data simulating a SBLOCA(tests 1008, 1010). It is suggested in [10] that $M_3(\alpha)$ may be useful in analyzing small pipe breaks where significant head degradation does not take place due to the lower voids present and the longer duration of the transient. A third correlation $M_M(\alpha) = \frac{h_{1\phi}-h_{tr}}{h_{1\phi}-h}$ developed from semi scale isothermal tests performed at Idaho Laboratories (tests 5-01-4A and 5-01-5) simulating a LBLOCA. To study the effect of pump degradation on transient results, all three correlations have been inputted.

3.2.4 Steam generator

Coolant from the reactor outlet header flows into the semi-spherical steam generator inlet head where it is distributed amongst 4663 inverted U-tubes with inner diameter 0.0136 m, and thickness of 0.00114 m, composed from Inconel 800 [8]. The U-tubes are modeled as an equivalent pipe using the parallel averaging formulas discussed in section 3.1. On the secondary side, feedwater is directed through the feed-in nozzle into the pre-heater section. Approximately 15% of the nozzle flow reaches the lower boiler section through the thermal leakage plate located at the bottom of the steam generator. The remainder of the feedwater is directed upward in the pre-heater section where it flows through six semicircular baffles before reaching the upper boiler section. Following the modeling in [20], the flow through the thermal plate is modeled as coming directly from the feed-in nozzle. As most of the wetted perimeter is composed of the U-tubes' outer perimeter, the surface roughness of the U-tubes corresponding $1.5 * 10^{-6}$ m is used for the pre-heater, lower boiler and upper boiler sections of the steam generator. Due to the irregular flow path of the pre-heater section, the appropriate minor loss may be estimated from boiler operating conditions as follows:

Feed water enters at the bottom of the pre-heater section at 177° C and a pressure of approximately 5200 kPa[20], and reaches saturation (Tsat=266.4° C) by the time the flow reaches the top of the pre-heater section. As the hydraulic diameter and flow areas in the upper steam generator sections are fairly large, it is reasonable to assume that the pressure drop due to major and minor losses in these sections is negligible. The pressure at point 2 may then be calculated by summing the hydrostatic pressure $\Delta P_{hydro-static} = \rho g \Delta z$ with the boiler design pressure in the separator section (P=5068 kPa). The pressure at the top of the pre-heater section is therefore P=5068 kPa + 9.81*775.19*(16.053-3.62)=5162.548 kPa. The minor loss for the pre-heater section was then found through the application of Bernoulli's equation to have a value of $K = 1671$ Pa/Pa.

The flows from the lower boiler section and pre-heater sections merge together in the upper boiler section and flow amongst the outer perimeter of inverted U-tubes to the riser. A total of 104 centrifugal separators are placed at the top of the riser section. The two phase flow from the riser section is split amongst the separators. Vapor-liquid separation is achieved in two stages. The primary separators separate the bulk vapor from the liquid, while the secondary separators/dryers remove any droplets/bubbles remaining in the vapor core. The separation process is modeled using the simple separator component available in RELAP5. The separator component consists of three junctions; junction J_3 corresponds to the separator inlet carrying the steam-water mixture and is connected to the upper boiler section, junction J_2 represents the liquid fall back from the separator and is connected to the down comer, and junction J_1 corresponds to the vapor outlet and is connected to the steam dome. Two additional inputs are required for the separator component. VOVER is the vapor volume void fraction above which the flow out of the vapor outlet is pure vapor. VUNDER corresponds to the liquid volume void fraction above which the flow out of the liquid fall back is pure liquid [26]. The values for VOVER and VUNDER were varied until the appropriate vapor outlet mass flow and steam generator circulation ratio were reached.

Liquid level in the drum is controlled through the boiler level control system. A time dependent junction was used to model the feed in nozzle. The flow from the time dependant junction(flow boundary condition) is varied until the steam generator level set point is reached. The set point is calculated based on the reactor thermal power at steady state details of which are described below.

In the CANDU 900, reactor thermal power is calculated from the temperature and flow measurements of the forty four finch channels[19]. In the RELAP simulations, flow and temperature measurements are obtained based on measurements from the average channel. The channel outlet quality x may be calculated from:

$$x = k_1(1 - \frac{\dot{m}_{outlet}}{\dot{m}_{inlet}}) \tag{3.14}$$

where $\dot{m}_{outlet}$, $\dot{m}_{inlet}$ are the coolant flow rates in kg/s at the outlet feeder and at the inlet feeder respectively and k_1 has a value of 0.0788[12]. Channel thermal power is then calculated as:

$$P_{channel} = W_{inlet}(K_2 + K_3(2T_{inlet} + \Delta T) + K_4 x) \tag{3.15}$$

where the constants K_2, K_3, K_4 are given as[12]:

K_2=	0 kW/(kg/s)
K_3=	0.009 kW/(kg/s)/ $\circ C$
K_4=	1215.0 kW/(kg/s)

Boiler level set point is then calculated from the average channel power as[3]:

$$P_{set} = C_1 + C_2\sqrt{P_{channel}} \tag{3.16}$$

and the constants C_1 and C_2 have values of 2.1 m and 0.227 m/$\sqrt{(\%FP)}$[4].

A governor valve at the top of the steam generator connects the main steam line to the turbine, and controls the steam generator operating pressure. The turbine is modeled as a time dependent volume with the appropriate boundary condition. A servo valve is used to model the governor valve. Valve stem position is controlled based on a proportional plus integral controller driven by the boiler pressure error defined as $E_{\text{SG-pressure}} = P_{\text{set}} - P_{\text{steam-dome}}$. P_{set} is taken to be the design operating

---

[3] Reference [21],subroutine blcdig.f

[4] Reference [20], CV14

pressure of 5068 kPa[8].

3.2.5 PHTS Pressure Control

All large nuclear power plants are designed for base-load service[25]. Hence, the chief concept of the control system in CANDUs is that the reactor pressure be maintained approximately. This is achieved through the pressure and inventory control system. The purpose of the system is to sustain a specific system pressure, and a specific level of inventory in the heat transport system. System pressure is controlled through the pressure of pressurizer. Pressurizer pressure is controlled by heat addition through six heaters placed at the bottom of the pressurizer, or by bleeding heavy water vapor from the pressurizer to the bleed condenser through the steam bleed valve. Two modes of control exist for the HTS pressure and inventory control system; the "narrow range"[12] control program is activated when the reactor is operating at power, and the "wide range"[12] control program is activated when the reactor is shutdown and the heat transport system is either warming up or being cooled down. The control program is executed every two seconds. The details of the "narrow range" control program are discussed below.

The pressure error E_{PROH} is calculated as the difference between the maximum of the four reactor outlet header pressures P_{ROH} [5] and the pressure set point P_{set} provided in [20]. The error dead band is reported in CV2 of [20] to be equal to $E_{db} = 30$ kPa. The valve demand on the steam bleed valve is then calculated from the pressure error $E_{\text{PROH}} = P_{\text{ROH}} - P_{\text{set}}$ as[6]:

$$\text{if } E_{PROH} \leq E_{pdb} \qquad \text{Valve Demand} = 0$$

$$\text{if } E_{PROH} \geq E_{pdb} \qquad \text{Valve Demand} = \text{GAIN} * (E_{\text{PROH}} - E_{\text{db}})$$

---

[5] Reference [21], subroutine anlgcn.f lines:75-79

[6] Reference [21], subroutine anlgcn.f

where valve demand gain on the error is reported in CV2 of [20] to have a value of GAIN = 0.004 valvelift/kPa.

In the case that system pressure is below the given set point pressure, heat is added through five on/off and one variable heater to increase overall system pressure. Each heater is assumed to have a maximum power of 250 kW [7]. A minimum pressure level below which the heaters are turned off is given [8] as $L_{\text{min}} = 0.8$ m. In addition to the pressure error, a temperature error is also used to derive the heaters. For pressures greater than 8901.0 kPa, the saturation temperature $T_{SAT,ROH}$of the reactor outlet header is calculated at each program execution as[9]:

$$T_{SAT,roh} = b + a(P_{\text{ROH}} - c) \tag{3.17}$$

where a, b, and c, are reported in [20][10] to have values of 0.0075727 °C/kPa, 301.67 °C, and 8901.0 kPa respectively. The temperature error may then be calculated as the difference between the header temperature T_{ROH} and the saturation temperature such that[11] :

$$E_{\text{temp}} = T_{SAT,ROH} - T_{\text{ROH}} \tag{3.18}$$

The variable heater power demand is then calculated from[12] as:

$$\begin{aligned} Q_{VH} &= G_1 E_{\text{PROH}} + G_2 E_{\text{temp}} \quad && \text{for } P_{\text{ROH}} \geq 8901 \text{ kPa} \\ Q_{VH} &= 0 && \text{else} \end{aligned}$$

The pressure and temperature controller gain variables are calculated from inputs of the CV17 card in [20] to have values of $G_1 = \frac{3.0\text{kW/kPa}}{250\text{kW}} = 0.012$ 1/kPa, and

---

[7] Reference [20], CV17

[8] Reference [20], CV17

[9] Reference [21], subroutine anlgcn.f:lines 241-244

[10] CV17

[11] Reference [21], subroutine anglcn.f

[12] [21], subroutine anglcn.f:lines 243-258

$G_2 = \frac{600\text{kW}/^\circ\text{C}}{250\text{kW}} = 2.4\ 1/^\circ\text{C}$.

Variable heaters are turned on $Q_{O/F} = 1.0$ if the reactor outlet pressure drops below 9851 kPa, and the temperature error is greater than the minimum temperature error of 2.8 °C[13]. Both the variable heater's gain Q_{VH} and the on/off heaters' gain $Q_{O/F}$ are overwritten to zero if the pressurizer water level is lower than $L_{min} = 0.8$ m[14]. The total power to be supplied to the heaters can then be calculated from:

$$P_{HEATERS} = 250\text{kW} * [Q_{VH} + 5 * Q_{O/F}](1 - Q_{\text{LOST}}) \tag{3.19}$$

where Q_{LOST} is the fraction of the power considered lost to the environment and is reported as $Q_{\text{LOST}} = 0$ kW in [20][15]. The heaters are assumed to be accurately represented as first order instruments with a time delay of $t_s = 37.5$ s[16]. Actual heater power P at each time-step is then calculated from the solution of[32]:

$$\frac{dP}{dt} - \frac{P}{t_s} = \frac{P_{HEATERS}}{t_s} \tag{3.20}$$

The heaters are modeled as a heat structure connected to the lower section of the pressurizer with the power calculated from equation 3.20 deposited directly to the coolant so that no heat conduction is modeled.

The water level in the pressurizer provides an indication for the total HTS coolant inventory. The heat transport feed and the heat transport bleed valves connecting the reflux condenser to the primary heat transport system are used to add and remove coolant from the system. As the presence of of the HT inventory control system does not contribute to the transient results (flow from the system is less than 10kg/s under normal operating conditions), the inventory level control system is not accounted for

---

[13] Reference [20], CV17

[14] Reference [20], CV17

[15] CV17

[16] Reference [20], CV17

in the RELAP5 model. Instead, the pressurizer is connected to a time dependant volume through a time dependant junction. Coolant is added or removed from the HTS to/from the time dependant volume until the appropriate pressurizer level is reached at steady state. The time dependant volume is then isolated from the HTS by setting the flow from the time dependant junction to zero at the start of the transient. The pressurizer set point level L_S is calculated based on the reactor linear power P_{LINM}. In order to account for the time lag involved between the power measurement and the pressurizer water swelling, a linear filter is applied to the linear power(given in terms of fraction of full power). The filtered power at the new time step P_{JN}^n is calculated from[17]:

$$P_{JN}^n = [1 - \frac{T_s}{T_{CPFLT}}]P_{JN}^{n-1} + \frac{T_s}{T_{CPFLT}}P_{\text{LINM}} \tag{3.21}$$

where the constants T_s, and T_{CPFLT} are the sampling time and filter calculation time[18] provided in CV4 of [20] are taken to be equal to to 2s and 10s respectively. The level set-point may then be calculated from the table below[12].

P_{JN}	Set Point L_S in m
0	3.640
0.86	5.910
0.91	6.105
1.0	6.750
≥ 1.03	7.0264

Table 3.18: Pressurizer level set-point in terms of reactor linear power

---

[17] Reference [21], subroutine anlgsb.f line 135

[18] Reference [21], subroutine anlgcn.f lines 199 -204

3.2.6 Point Kinetics Model and SDS1

Power measurements are simulated using a point kinetics model. Reactor power is computed from the point kinetics approximation assuming that the reactor power may be represented by the product of a space and a time function. As a consequence of this approximation, it is assumed that the relative power distribution remains the same as that under normal operating conditions, and that the effect of the shutdown system can be accurately expressed as a function of the bulk reactor reactivity. Changes in reactivity can be considered as internal(reactivity resulting from changes in fuel temperature, coolant temperature, and coolant voiding) and external(reactivity resulting from shut-down rods, zone controllers, and adjuster rods). Moderator temperature feedback effects are not modeled as little heat transfer takes place between the pressure tube and the calandria tube during the early blowdown period and a constant moderator temperature may be assumed.

Two main factors contribute to fuel temperature reactivity[34]:

1. Neutron Spectrum Effect: A change in fuel temperature results in an effective change in the temperature of the neutrons in the fuel. An increase in fuel temperature results in the the peak of the thermal neutron spectrum to decrease, with the average of the most probable neutron density to increase. The reproduction factor in the six factor formula is most affected by this phenomena.

2. Doppler Effect: An increase in fuel temperature results to a lower resonance escape probability due to the increase capture of neutrons by ^{238}U, resulting in an overall decrease in reactivity.

As suggested in reference [33], a second order polynomial interpolation was used to generate the graph. The uncertainty of ±20% is assumed for fuel temperature reactivity.

Reactivity changes due to coolant voiding in the core stem from[35]:

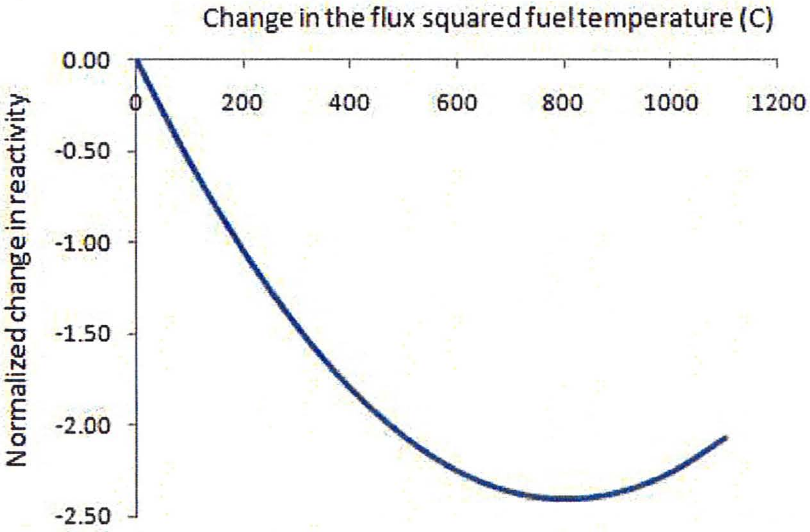

Figure 3.11: Change in reactivity due to fuel temperature

1. Fast Fission Factor: Under normal operating conditions, the coolant acts as a moderator for high energy neutrons, thereby reducing the occurrence possibility of fast fission with ^{238}U. Voiding of the coolant results in an overall increase in the rate of fast fission with ^{238}U resulting in an increase in reactivity.

2. Resonance Absorption Factor: Neutrons of thermal energy are up-scattered by the coolant into the low resonance capture energy range of ^{238}U and ^{239}Pu. Thermal absorption in ^{238}U are parasitic, while absorption by ^{239}Pu may lead to fission. Coolant voiding has the effect of decreasing the low resonance capture with an overall effect of a positive change in reactivity. The effect is reduced with increasing burn-up due to the increase in ^{239}Pu concentration.

The reactivity change for complete voiding of one loop(half core void) is reported to be 8.2 mk[19]. This is taken to be 52% of the reactivity change for a fully voided core. Reference [33] suggests that the dependence of Δk_{void} with respect to core void is linear with $\Delta k_{void} = 0$ at $\rho_{core} = \rho_{ref}$ where ρ_{ref} is the core density at the start of the transient. The core coolant density ρ_{core} can be calculated from[33]:

$$\rho_{core} = \frac{\sum_i V_i \frac{\sum_j \rho_{ij} P_{ij}^2}{\sum_j P_{ij}^2}}{\sum_i V_i} \tag{3.22}$$

where ρ_{ij}, and P_{ij} are the density, and power at node j of group i respectively. The average core void α_{core} can be approximated from:

$$\alpha_{core} = 1 - \frac{\rho_{core}}{\rho_{ref}} \tag{3.23}$$

An uncertainty of $\sigma = \pm 2$ mk is assumed for coolant void reactivity.

Two independent shutdown systems (SDS1 and SDS2) are used to shutdown the reactor in the case of a power excursion. The systems are set to activate when certain sensed parameters exceed their set point values. As SDS1 is activated prior to SDS2, only SDS1 will be modeled.

SDS1 employs 32 neutron absorbing rods into the reactor core. The rods are in the form of a steel-cadmium-stainless steel sandwich tube with a length of 5.72 m and an outer diameter of 112.7 mm [19]. The net reactivity worth (for equilibrium core) is reported in [19] to be -71 ± 3 mk for insertion all 32 rods, and -51.3 ± 2 mk with the two most effective rods removed. Two factors contribute to the net reactivity worth of the shutoff rods: those associated with the prediction of the position of the rods as they move through the moderator, and those associated with the reactivity worth of the shutoff rods in the core for a given position. Figure 3.2.6 compares the tabulated sopht data for the net reactivity worth of the shutoff rods to those for a 100% pump suction and a 20% reactor inlet header. As can be seen from the figure, the impact of the core's flux distribution change from the reactor's equilibrium conditions on the net reactivity worth of the shutoff rods is minimal. The minor differences are most likely due to updated calculations for rod insertion rate. An uncertainty of ±1mk is

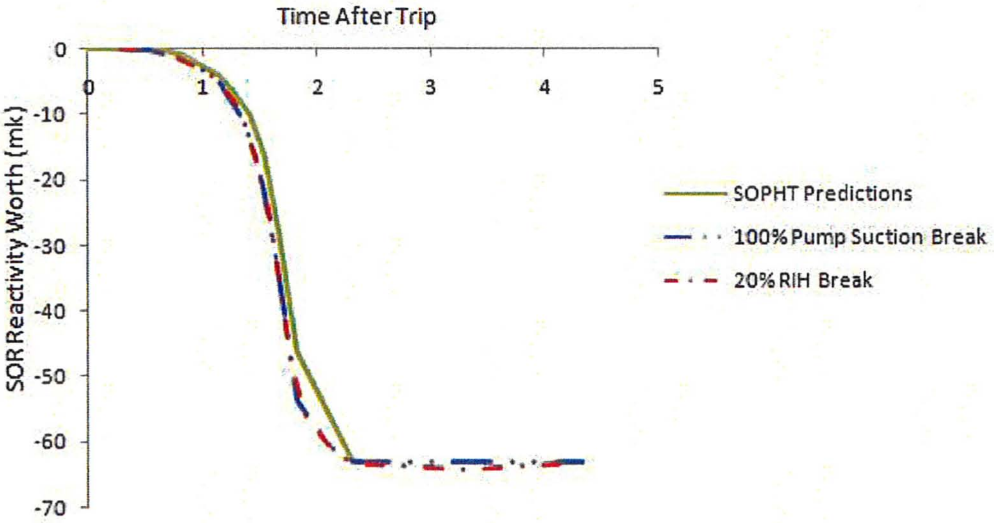

Figure 3.12: SDS1 normalized reactivity vs. time after trip

chosen to be applied to the shutoff rods reactivity worth.

Two trips are considered for SDS1. The Neutron Over Power Trip (NOP) compares the sensed reactor power measured from in-core neutron flux detectors to a set point of 1.20% FP for SDS1. In the RELAP5 model, two transformations of the form of equation 3.20 modeling first order instrument delays, are applied to the fission power calculated from the reactor kinetics module. The result is compared to the power set point. A trip time delay of 0.30 ms is added to simulate the delay between the trip activation and SDS1 initialization. The set point uncertainty is assumed to be an unbiased normal with $\sigma = 3/4 = 0.75\%$.

The High Power Log Rate(HLR) trip compares the rate of the reactor log power measured from in core ion detectors to a set point of 0.15% FP/s. In the RELAP5 model, two transformations of the form of equation 3.20 are applied to the rate of the logarithm of the fission power. The result is compared to the set point.

The table below lists the time constants τ_1, τ_2 for NOP and HLR trips.

Trip	τ_1	τ_2

NOP	0.2 ms	0.2 ms
HLR	180 ms	190 ms

The fission power $P_f(t)$ is calculated from the solution of the point kinetics equations:

$$\frac{1}{Q_f}\frac{d}{dt}P_f(t) = \frac{[\rho(t)-\beta]\psi(t)}{\Lambda} + \sum_{i=1}^{6}\lambda_i C_i(t) + S \tag{3.24}$$

$$\frac{d}{dt}C_i(t) = \frac{\beta f_i}{\Lambda}\psi(t) - \lambda_i C_i(t) \tag{3.25}$$

$$P_f(t) = Q_f\psi(t) \tag{3.26}$$

where Q_f is taken to be 200 MeV/fission. The delayed neutron fraction for group i β_i and time constants λ_i are reported in [33] and are reproduced below. These values describe the life time and relative amplitudes of neutrons produced as result of beta decay of fission products and emissions of photoneutrons through (γ, n) reactions. The total neutron fraction β_{eff} is reported in [33] to have a value of 0.00582. The uncertainty for contribution from fission product beta decay with the released neutrons in the energy range of 0.5-4 MeV for fissions in ^{235}U and ^{239}Pu are reported in reference [39] as 3.5 %, and 4.1 % respectively. The larger of the two uncertainties is assumed. The same uncertainty is assumed to apply for the contribution of photoneutrons to total delayed neutron fraction. The overall contribution of the photoneutrons is approximately 5% [36]. The uncertainty for the delayed neutron fraction is therefore taken $\sigma = \sqrt{(0.95 * 4)^2 + 0.5 * 4^2} = 4.6\%$. The normalized delayed fractions for each group along with their respective time constants are provided in the table below[33].

group	normalized β_i	λ_i s^{-1}
i=1	0.050687285	0.000612
i=2	0.200171821	0.03155

i=3	0.177491409	0.1218
i=4	0.403780069	0.3175
i=5	0.134020619	1.389
i=6	.033848797	3.784

The prompt neutron generation life time is reported in [33] as $\Lambda = 0.902 * 10^{-3}$s for equilibrium fuel. This parameter is dependent on neutron velocities in the fast and thermal energy regions. Since neutrons generally spend most of their lifetimes in the thermal region, the accuracy of the thermal neutron velocities has a greater effect on the data. Unfortunately, no data in open literature was found to calculate the uncertainty ranges for the generation lifetime. A normal with a standard deviation of $\pm 5\%$ is assumed.

3.3 Uncertainty Analysis for Plant Operating Parameters

The use of a limited set of data with n points to represent the entire data set results in sampling error. The sampling error for a calculated statistic (mean, standard deviation) can be approximated to a set confidence level C through the theories of statistical inference. If the distribution is normal, the parent population mean μ can be found for a given confidence interval, using the sample mean $\bar{\mu}$ and the sample deviation $\bar{\sigma}$ from[41]:

$$t_{C,n-1} = \frac{\mu\sqrt{n}}{\bar{\mu}} \tag{3.27}$$

where $t_{C,n-1}$ has a known distribution $p(t)$ called the *Student t-distribution* with n-1 degrees of freedom.

Similarly the standard deviation σ of the parent population is related to the sample standard deviation $\bar{\sigma}$ through[41]:

$$\sigma = \bar{\sigma}(\frac{n-1}{\chi^2})^{\frac{1}{2}} \tag{3.28}$$

where χ^2 follows the chi-squared distribution with $n-1$ degrees of freedom.

3.3.1 Bulk Reactor Power

Figure 3.3.1 shows the bulk reactor observed power in terms of % FP. The observed data variation for bulk reactor power is assumed to follow a normal distribution with mean of $\bar{\mu} = 99.84$ % FP and a standard deviation of $\bar{\sigma} = 0.0954$ % FP. The one sided error estimates with 95 percent confidence for the mean and the standard deviation are calculated to be 0.0093 and 0.0016 % FP respectively and are too small to have any significant contribution. Error distribution for the measuring instrument

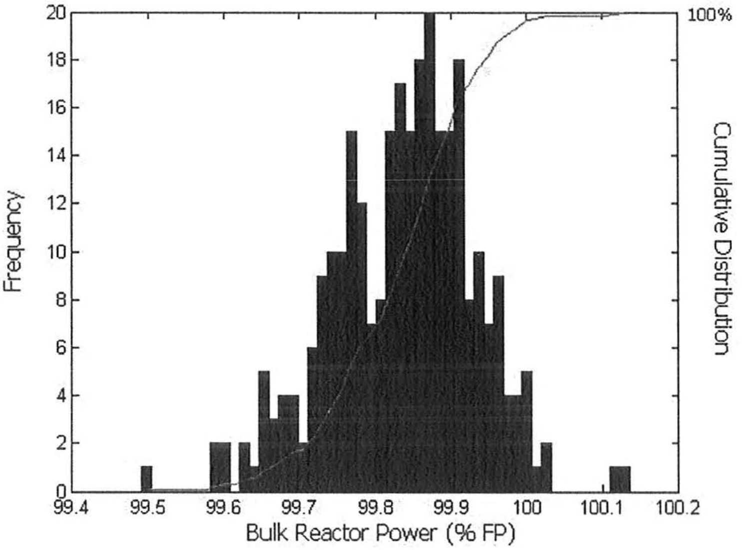

Figure 3.13: Observed bulk reactor power distribution

uncertainties are not available. The measurement error is assumed to be normally distributed with a standard deviation of 0.5% FP. A 1.5% bias [44] is assumed for the reactor bulk power.

3.3.2 Core-wide Maximum Channel Power

At Darlington NGS, the license limit states that "The total power generated in any fuel channel of the reactor core shall not exceed 7.2 megawatts under normal steady-state operating conditions." [42] This compliance is achieved through the estimation of channel powers either by direct measurement of the FINCH channels or computation. In both cases, the estimated powers suffer from uncertainties. This analysis uses simulation results from the SORO code for Darlington Unit 1 over the period of December 31, 2007 to October 29, 2009. The SORO code calculates the channel specific powers for the 480 channels of the Darlington Core. The SORO error is defined as the relative ratio of the difference between the calculated SORO channel powers $\{S_1, S_2, ..., S_{480}\}$ and the true channel powers $\{Q_1, Q_2, ..., Q_{480}\}$ to the true channel powers such that:

$$S_i = Q_i(1 + \epsilon_i) \text{ for } i = 1, 2, ..., 480 \tag{3.29}$$

The SORO error for each channel ϵ_i may then be decomposed into a core common reactor power ϵ_{RP} and a channel specific FLUX error component ϵ_{FLUX} such that $\epsilon_i = \epsilon_{RP} + \epsilon_{FLUX}$. Traditionally, the simulation error was accounted for by taking both errors to be at their maximum and simply adding the maximum error to the results. For example, if the simulation error uncertainty (accounting for the measurement errors) is σ then the maximum uncertainty is taken to be $z_\alpha \sigma$, where z_α is the 100(1-α) percentile point of the standard normal distribution. For Darlington, the SORO simulation error is reported in [42] as $\sigma = 1.71\%$[42], then for the 95th percentile, the maximum uncertainty of $2\sigma = 3.58\%$ may be used. Such treatment of the maximum channel power uncertainty leads to unnecessarily conservative MCP compliance. Reference [42], formulates an algorithm for calculating the least upper bound of the maximum error for the $(1 - \alpha) * 100^{th}$ percentile point . The details of the algorithm are as follows[42]:

1. For a given reactor state, $\{Q_1, Q_2, ..., Q_{480}\}$ are the SORO computed channel powers. Let $Q_{max} = \max\{Q_1, Q_2, ..., Q_{480}\}$
2. For t=1,2,3,4,...,N do
    (a) choose ϵ_{RP} randomly a normal distribution with a standard deviation of σ_{RP}
    (b) choose $\epsilon_{FLUX,i}$ randomly a normal distribution with a standard deviation of $\sigma FLUX$ for each of the $i = 1, 2, ..480$ channels
    (c) let $\epsilon_i = \epsilon_{RP} + \epsilon_{FLUX,i}$

   (d) let $S_i = Q_i(1 + \epsilon_i)$

   (e) let $S_{max} = \max\{S_1, S_2, ..., S_{480}\}$

   (f) let $\eta_t = (S_{max} - Q_{max})/Q_{max}$

3. Sort the sample $\{\eta_1, \eta_2, ..., \eta_N\}$ in the ascending order. The resulting sample is $\eta_{(1)}, \eta_{(2)}, ..., \eta_{(N)}$

4. For a given α, compute an estimate $\bar{\eta_\alpha}$, of the optimal maximum uncertainty from $\bar{\eta_\alpha} = -\eta_{\alpha N+1}$

The number of simulations N is determined by considering an error of the computed percentile whose standard deviation is[42]:

$$\sigma_\alpha = \sqrt{\frac{\alpha(1-\alpha)}{N}} \tag{3.30}$$

For example, for $N = 100,000$ and $\alpha = 0.05$, then $\sigma_\alpha = 0.068\%$. In the above analysis, $\sigma_{RP}, \sigma_{FLUX}$ were taken to be 1% and 1.39% respectively(for Darlington Unit1)[42]. Data for 136 reactor states covering the mentioned periods have been conglomerated to get an overall estimate for η_α.

Repetition of the above algorithm for various values of α leads to a cumulative distribution function for the maximum channel power error. The distribution of the maximum channel power errors can be accurately represented as a normal with standard deviation of 1.5% with zero skewness.

3.3.3 Core Wide Maximum Bundle Power

The figure below shows a histogram of 136 SORO calculated states for the core-wide maximum bundle power over the period of December 31, 2007 to October 29, 2009 for Darlington Unit 1. The data is found to conform to a normal distribution with a mean of 801 kW and a standard deviation of 1.4 %.

Estimation of the bundle power error is a difficult task due to the lack of direct measurement data. Reference [43] outlines a methodology for estimating the SORO simulation error through comparison of the SORO simulated bundle powers with the irradiation dependent power bundle powers estimated from the POWDERPUFS' H and F factors for the 44 FINCH channels. The irradiation $\omega_{k,c}(t)$ for bundle k in channel c at time t may be defined as[43]:

$$\omega_{k,c}(t) = \int_0^t F[\omega(\tau)]\Phi(\tau)d\tau \tag{3.31}$$

where $F(\omega)$ is a flux depression factor accounting for the fact that the flux in the bundle is less than the thermal flux $\Phi(t)$. The bundle power is then defined as the rate at which a fuel bundle transfers its energy to the HTS and is given by:

$$B(t) = cH[\omega(t)]\Phi(t) \tag{3.32}$$

Where the coefficient c is the ratio of the generated thermal power to the produced fission power (taken to be 0.9) and the H-factor $H(\omega)$ is the bundle's fission power per cell-averaged thermal flux. Defining $y(\omega) = c\frac{H(\omega)}{F(\omega)}$, it is easy to show that:

$$B(t) = \omega'(t)y[\omega(t)] \tag{3.33}$$

where $\omega'(t)$ is the derivative of the irradiation with respect to time. The bundle power can therefore be calculated from the irradiation $\omega(t)$ and the function $y(\omega(t))$. The function $y(\omega(t))$ may be accurately represented as a 7^{th} order polynomial with coefficients calculated through the minimization of the error $\sum_{c\in F} ||M_{c,t} - Q_{c,t}||^2$ where $M_{c,t}$ is the measured channel power for each of the 44 finch channels and $Q_{c,t} = \sum_{k=1}^{13} BP_{k,c}(t) = \sum_{k=1}^{13} \omega'_{k,c}(t)y[\omega_{k,c}(t)] = \sum_{l=1}^{7} p_l \sum_{k=1}^{13} \omega'_{k,c}(t)\omega^l_{k,c}(t)$ is the calculated channel power. The individual bundle power errors $(W - BP)/BP$, where W is the SORO computed bundle power, and BP is the irradiation dependent calculated bundle power used to estimate the true bundle power are presented in [43]. It was found that essentially all bundle errors lie in the interval of ±10%. Furthermore, it as found that the error means generally decrease with increasing bundle positions. The systematic component of the error(mean error) is reported as 2.74% for bundle 6, with a irradiation dependent random component of $\sigma = 0.075$. In the current analysis, it is assumed that the maximum bundle power occurs at the center of the channel (bundles 6 and 7) with bundles at positions 6 and 7, having the maximum bundle powers.

3.3.4 RIH Temperature and ROH Pressure

As instrument uncertainties were not available for the measuring thermocouples, the values reported in reference [44] are used instead. Reference [44] reports the RIH temperature to be normally distributed with a mean of 265 °C and a standard deviation of 0.17. Similarly the ROH pressure is reported to have a normal distribution with a mean of 9.8 MPa and a standard deviation of 0.019.

3.3.5 Evaluation of Interdependence

The existence of interdependence between various operating parameters must be taken into account for the integrated uncertainty analysis. For example, under normal operating conditions the heat transport system pressure is dependent on the total inventory mass, and the energy of the system. Therefore, it may be expected that the reactor outlet pressure and the reactor inlet temperature are correlated. A good measure of the dependence of two parameters x and y is the Pearson correlation coefficient, defined as:

$$r_{x,y} = \frac{\sum_{i=1}^{N}(x_i - \bar{x})(y_i - \bar{y})}{\sqrt{\sum_{i=1}^{N}(x_i - \bar{x})^2 \sum_{i=1}^{N}(y_i - \bar{y})^2}} \tag{3.34}$$

where $\bar{x}, \bar{y}$ are the means of the sample data sets $\{x_i\}$, $\{y_i\}$ respectively. The coefficient $r_{x,y}$ has values between ±1 with the values in the range of $|r_{x,y}| \leq 0.5$ indicating a weak correlation. The correlation coefficient for RIH temperature and ROH pressure have been calculated from data corresponding to the Darlington Unit4 operation on May 05, 2008, December 11, 2008 and December 11, 2009. Three measurements for each variable are available from three independent measuring instruments for each header. The median value is used as the representing value for each data set. The correlation coefficient for the three days of operation for each of the corresponding quadrants have been calculated and are presented in the table below.

Date	NE	NW	SE	SW
May 05, 2008	0.2798	0.1949	0.0202	0.1986
December 11, 2008	0.0867	0.1142	0.0809	0.0028
December 11, 2009	-0.0403	0.2504	-0.0096	0.2487

As seen, the maximum calculated value of the correlation coefficient is 0.27 indicating a weak correlation between the two parameters. This should be expected as the reactor outlet pressure is controlled by the pressure control system.

Another pair of parameters that may be correlated are the core-wide maximum channel power and maximum bundle power. The channel power is the sum of the powers produced by each of 13 bundles in the channel. Therefore, the maximum bundle power (channel specific) is expected to be strongly correlated with the channel power. However, in this analysis, it is assumed that the core-wide maximum channel and bundle powers occur in the same channel. This is usually not the case and there is little reason to believe why the two should be correlated. The correlation coefficient for the maximum channel power and bundle powers calculated from the SORO simulations corresponding to operation of Darlington Unit1 over the year of 2008 is calculated to be equal to 0.27, indicative of no strong correlation between the two parameters.

3.4 Uncertainty Data for Modeling Parameters

3.4.1 Wall to Fluid Heat Transfer

If a solid surface is defined as having a convective boundary attached to it, the heat transfer coefficients are calculated and passed on to the conduction solution. The general expression for the heat flux is given as[29]:

$$q''_{total} = h_{wgg}(T_w - T_g) + h_{wgspt}(T_w - T_{spt}) + h_{wgspp}(T_w - T_{spp}) + h_{wff}(T_w - T_f) + h_{wfspt}(T_w - T_{spt}) \tag{3.35}$$

where:

h_{wgg}= htc to vapor/gas, with the vapor/gas temperature as the reference temperature (W/m^2 K)

h_{wgspt}= htc to vapor/gas, with the saturation temperature based on the total pressure as the reference temperature (W/m^2K)

h_{wgspp}= htc to vapor/gas, with the saturation temperature based on the vapor partial pressure as the reference temperature (W/m^2K)

h_{wff}= htc to liquid, with the liquid temperature as the reference temperature (W/m^2K)

h_{wfspt}= htc to liquid, with the saturation temperature based on the total pressure as the reference temperature (W/m^2K)

T_w= wall surface temperature (K)

T_g= vapor/gas temperature (K)

T_f= liquid temperature (K)

T_spt= saturation temperature based on the total pressure (K)

T_spp= saturation temperature based on the partial pressure of vapor in the bulk (K)

Usually for most flow regimes only one or two of the heat transfer coefficients in the above equations are non-zero.

Pre-CHF Heat Transfer

The heat transfer coefficient used by RELAP5 for single phase forced convective heat transfer is the Dittus-Boetler correlation. The correlation has the form [29]:

$$\frac{h_{sp}}{D}k = CRe^{0.8}Pr^{n} \tag{3.36}$$

where h_{sp} is the single phase heat transfer coefficient and the value of $C = 0.023$[52] with the exponent of the Prandtl number $n = 0.4$ is used in the code. The range of conditions for the data used in deriving the Dittus-Boelter correlation was found to have a scatter of 40% [52, 29]. The uncertainty is therefore modeled as an unbiased normal having a standard deviation of 40%.

The correlation proposed by Chen[29] is used for the nucleate boiling model. Details of the model can be found in references [2]. The Chen correlation calculates the heat flux as a weighted average of the heat flux due to forced convection (macroscopic convection term) and the heat flux due to nucleate boiling (microscopic boiling term) and has the following form[29]:

$$q^{''} = h_{mac}(T_w - T_{spt})F + h_{mic}(T_w - T_{spt})S \tag{3.37}$$

where

$F = 2.35(\chi_{tt}^{-1} + 0.213)^{0.736}$ comes from the inverse Lockhart-Martinelli factor χ_{tt}

$\chi_{tt}^{-1} = (\frac{G_g}{G_f})^{0.9}(\frac{\rho_f}{\rho_g})^{0.5}(\frac{\mu_g}{\mu_f})^{0.1}$
and the suppression factor S is dependent on the F factor.

The macroscopic forced convection term h_{mac} is given by the Dittus Boelter equation (3.36) and the microscopic boiling term is calculated from[29]:

$$h_{mic} = 0.00122(\frac{k_f^{0.79} C_{pf}^{0}.45 \rho_f^{0.49} g_f^{0.25}}{\sigma^{0.5} \mu_f^{0.29} h_{fg}^{0.24} \rho_g^{0.24}}) \Delta T_w^{0.24} \Delta P^{0.75} \tag{3.38}$$

Note that in the subcooled nucleate boiling region, the subcooled liquid conditions are used for the convection term so that $T_w - T_{liquid}$ is used in equation (3.37) instead of $T_{wall} - T_{spt}$. The correlation has been applied to both water and organic fluids covering a range of:

Pressure	0.05-3.48 MPa
Liquid Velocity	0.06-4.5 m/s
Quality	1-59 %
Heat Flux	41-240 kW/m^2

The uncertainty in the data is tabulated in reference[29] with a maximum scatter of 15.4%. The model uncertainty is therefore taken to be an unbiased normal with a standard deviation of $\sigma = 15.4\%$.

CHF Multiplier

The encountered high void fractions and mass flows result in the annular dispersed regime, where a thin liquid film covers the walls while vapor and entrained droplets move at a higher velocity in the core. In this regime, a continuous thinning of the liquid film occurs, caused by entrainment of the liquid (in the core region) and evaporation at the interface as a result of conduction through the film. The film thickness decreases along the length of the pipe and with increasing heat flux until eventually entrainment is suppressed. An imbalance between the rate of droplet deposition and the rate of evaporation results in the breakdown of the film. This results in a moderate surface temperature rise.

Two mechanisms promote this liquid film breakdown[5]. At low flows and high qualities, surface tension forces at the wavy interface dominate. Surface tension gradients draw the liquid to areas of high surface tension and the liquid film will eventually break down in the valley of the wave. If film thickness is comparable to the maximum possible bubble size, then a momentary drypatch may occur resulting from a possible bubble rupture at the interface. The heat flux at which dryout occurs is referred to as the Critical Heat Flux(CHF), and is usually calculated based on correlations derived from steady state tests correlating the heat flux with local thermohydraulic properties such as pressure, mass flux and equilibrium quality. RELAP5 calculates the critical heat flux from interpolation of the 1986 AECL-UO CHF lookup table developed by Groeneveld using data for tube geometries. The correlation has the form [29]:

$$CHF = CHF_{table} * k_1 * k_2 * k_3 * k_4 * k_5 * k_6 * k_8 \tag{3.39}$$

where k_1 to k_8 are correction factors accounting for bundle geometry and are defined in [29]. For pressures above 1 MPa, the data from which the correlation was derived was found to have an RMS error[6] of 52.7%[19]. At higher pressures and lower heat fluxes encountered in CANDUs the uncertainty in the correlation is cited as 10% in reference [6]. The CHF correlation as applied in the code has three other sources of uncertainty associated with it; An additional 5% error arises from applying tube data with the appropriate multiplied correction factors to estimate CHF in bundle geometries[5]. In addition, the deriving data for the correlation was obtained from steady state tests. The application of data from steady state tests to transient analysis is investigated in [4] and was found to estimate the data reasonably well, with an uncertainty of ±25% (taken as 2σ) for most tests. Also, note that the modeling is based on the assumption that the CHF occurs simultaneously across a bundle while in reality [5] states that in a 37 element bundle, "it requires typically 50% increase power (for the same local flow conditions, P, G, X) to have the CHF spread across the half the bundle geometry and over 100% to spread across the whole geometry." The uncertainty is therefore taken to be a normal distribution with a bias of 50% (required for 95% of the bundle to dryout), and a standard deviation of $\sigma = \sqrt{10^2 + 5^2 + (\frac{25}{2})^2} = 16\%$

Post CHF Heat Transfer Coefficent

Upon reaching dryout, the amount of contact between the liquid and the wall is reduced leading to a reduction in the heat transfer coefficient and an gradual increase in the surface temperature. Evaporation of the liquid as a result of this increase in heat flux results in a rapid transition of the two phase flow conditions to that of single phase vapor. Heat transfer mechanisms during this transition consist of heat transfer to liquid in direct contact with the wall, heat transfer to the liquid by radiation, heat transfer to the vapor blanket via conduction, convection to the flowing vapor and heat transfer between the vapor and the dispersed droplets. Chen's transition boiling correlation and Bromley's film boiling correlations are used by RELAP5 to calculate

---

[19] When using the Direct Substitution Method

the heat flux in this region. The heat flux value is taken as the larger predicted value by the two models.

Chen's transition boiling model ignores heat transfer to the liquid by radiation(reported in [29] to be less than 10%) and assumes that the total boiling heat transfer coefficient is a sum of heat transfer to the liquid in contact with the wall, and heat transfer to the vapor phase. The correlation has the form [29]:

$$q_{tb} = q_{CHF}A_f + hg_g(T_w - T_g)(1 - A_f) \tag{3.40}$$

where A_f is the empirically calculated fraction of wall wetted area and is dependent on the probability of the liquid contacting the walls at each point, and $hg_g = 0.0185Re^{0.83}Pr^{1/3}$ is the vapor heat transfer coefficient suggested by Colburn. The correlation has been successfully to experiments with a mean deviation of 16.0% covering a range of [29]:

Pressure: 0.42-19.5 MPa
Mass flux G: 40.7-3526 kg/m^{2}s
Equilibrium quality x_{eq} : 0.151-1.728
Heat flux q$''$: 0.34-16.6 *10^5 W/m^2

The correlation uncertainty is therefore taken to be a normal distribution with a standard deviation of $\sigma = \sqrt{\frac{\pi}{2}} * 16.0\% = 20.1\%$.

Bromley's heat transfer correlation assumes that the repulsive force generated by the evaporating liquid is large enough not to permit any liquid contact with the wall. The conduction mechanism of the model is modeled as[29]:

$$hf_{spt} = 0.62[\frac{g\rho_g k_g^2(\rho_f - \rho_g)h_{fg}C_{pg}}{L(T_w - T_{spt})Pr_g}]^{0.25}M_a \tag{3.41}$$

where M_a is a correction factor based on the void fraction and takes a value between unity for low void fractions and zero for high void fractions $\alpha_g = 0.999$. The deriving data was correlated to within ±18% which is taken as the standard deviation. The correlation uncertainty is therefore taken as an unbiased normal with a standard deviation of $\sigma = 18\%$.

3.4.2 Break Discharge Model

The discharge of a liquid at high pressure and temperature is governed by the compressible behavior of the liquid vapor mixture that is formed as the coolant is discharged to the ambient pressure. If the liquid is subcooled or saturated, expansion of the liquid from its stagnation conditions to those at the throat(flashing) gives rise to mechanical and thermal non equilibrium effects resulting in heat, mass and momentum transfer between the phases which characterize the flow. As the pressure in the header is decreased further, the point at which flashing occurs(saturation temperature is reached) is moved further upstream and eventually the flow is two phase by the time it reaches the throat. Ignoring wall shear forces, the maximum discharge (critical flow) G_c at any instance in time is related to the pressure drop ΔP between the upstream and the throat as[53]:

$$\Delta P = \frac{G_c^2 v}{2C^2} \tag{3.42}$$

where v is the upstream mixture specific volume and C is the orifice discharge coefficient and has the recommended value of 0.8[29]. A general one dimensional expression for two phase, one component critical flow is given in [29] as:

$$\begin{aligned}G_c^2 = -[k([1+x(k-1)]x\frac{dv_g}{dP} + \{v_g[1+2x(k-1)] \\ + kv_l[2(x-1)+k(1-2x)]\}\frac{dx}{dP} \\ + k[1+x(k-2)-x^2(k-1)]\frac{dv_l}{dP} \\ + x(1-x)(kv_l - \frac{v_g}{k}\frac{dK}{dP})^{-1}]_t\end{aligned} \tag{3.43}$$

where k is the slip ratio between the vapor and liquid phase and the subscript t indicates that the enclosed quantities are evaluated at the throat. Henry and Fauske[53] argued that for flows with low qualities or high pressure in which the flow is nearly homogeneous, mechanical non equilibrium between the phases may be ignored ($k \approx 1$). Furthermore, they ignore the wall shear forces in the momentum equation (isentropic process), giving the simplifying the above equation to[53]:

$$G_c^2 = \frac{-1}{x\frac{\partial v_v}{\partial P} + (1-x)\frac{\partial v_l}{\partial P} + (v_v - v_l)\frac{\partial x}{\partial P}_s} \tag{3.44}$$

where $v_v, v_l, x, \frac{\partial v_v}{\partial P}, \frac{\partial v_l}{\partial P}$, and $\frac{\partial x}{\partial P}_s$ need to be evaluated at the throat conditions. As there is little time for mass transfer, and assuming that heat transfer is negligible so that the liquid temperature remains constant throughout the expansion, the entropy and quality could be taken the same as the upstream conditions. The liquid may also be assumed to be incompressible and its specific volume equal to that of the upstream so that $v_{l,t} = v_{l,0}$. Additionally, the vapor specific volume could be evaluated from the isentropic expansion of a gas so that $P_0 {v_{v,0}}^\gamma = P_t {v_{v,t}}^\gamma$. While the overall heat transfer may be assumed to be negligible, due to the large temperature differences between the phases, local heat transfer rate at the throat cannot be ignored and $\frac{\partial v}{\partial P}_t$

cannot be evaluated by assuming an adiabatic process. Assuming that the vapor expansion process may be accurately represented as a polytropic process, the vapor specific volume is then evaluated from $\frac{\partial v_v}{\partial P}_t = \frac{-v_v}{nP}_t$ where n is the polytropic index derived by Tangren et al(1949)[55]. Henry[29] presented a correlation for the rate of interphase mass transfer in constant area ducts expressed as:

$$\frac{dx}{dP}_t = -[\frac{(1-x)\frac{ds_1}{dP} + x_0\frac{ds_v}{dP}}{s_{v,0} - s_{l,0}}] = N\frac{dx_{eq}}{dP}\Big|_t \tag{3.45}$$

where x_{eq} refers to the equilibrium quality at the throat and the factor N is calculated from $N = min[1, \frac{x_{eq.t}}{C_{ne}}]$. Substitution of the above terms into equation (3.44) results in the critical value of mass flux given as[53]:

$$G_c^2 = [\frac{x_0 v}{\eta P} + (v_v - v_{l,0})\{\frac{(1-x_0)N}{s_{v,eq} - s_{l,eq}}\frac{ds_{l,eq}}{dP} - \frac{x_0 C_{p,v}(1-\eta-1-\gamma)}{P_t(s_{v,0} - s_{l,0})}]\}^{-1} \tag{3.46}$$

To evaluate the pressure, equation (3.44) is coupled with the momentum equation and solved iteratively. The assumption of negligible mass transfer, but non negligible mass transfer rate implies that the quality at the throat is zero while vapor generation (assumed to occur at saturation) takes place at the throat. The original model developed by Henry and Fauske used the ideal gas law to calculate the vapor specific volume which results in a discontinuity at the transition point between subcooled and two phase choked flow . To remove this discontinuity, the vapor specific volume is always evaluated using the water-steam property tables in RELAP5. The discrepancy between the model implemented in RELAP5 and the original model developed by Henry and Fauske is smaller than the experimental error for the data upon which the model was originally developed and is deemed negligible[29].

Reference[1] presents a comparison between the Marviken Tests 14 and 25 experimental data and prediction of the Henry Fauske model using RELAP5. Inspection of the error histogram shows the error in mass flux predictions to be normally distributed with a standard deviation of $\sigma = 0.109$.

Chapter 4

Results

4.1 Critical Break Search

Modeling the break as instantaneous (assumed to open within $10^{-5}s$), leads to a momentary discontinuity in the pressure gradient term of the momentum equation. As a result, immediately following the break, RELAP5 predicts a pressure spike/wave propagating (at local sonic speed) upstream of the RIH to the rest of the HTS. The amplitude of this pressure wave is dependent on the time step size and the numerical scheme of the code with the explicit scheme giving higher values for the pressure wave amplitude (approximately 7 MPa) than the implicit scheme (6 MPa). Reduction in time step size was also found to decrease the amplitude of the pressure wave. The amplitude of this wave is found to have little effect on the overall HTS response as the predicted values for the recovered reactor header inlet pressure were found to be independent of the numerical scheme and time step sizes.

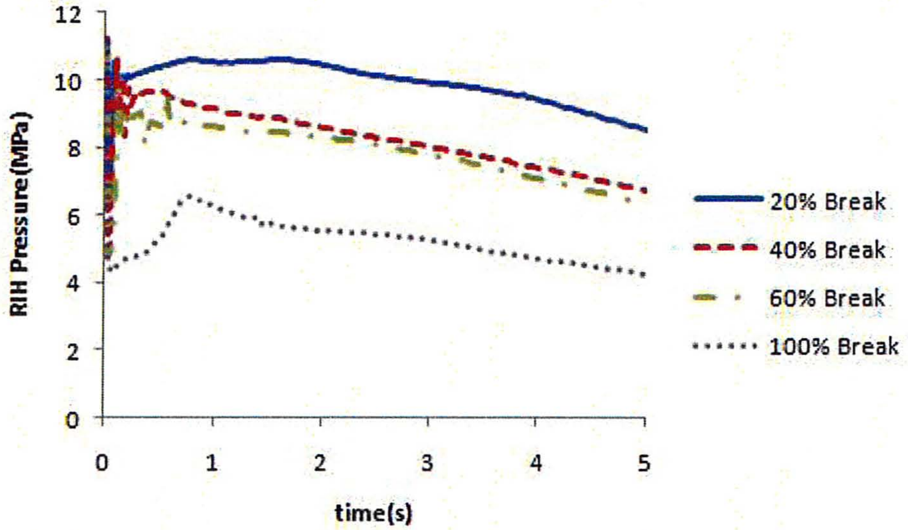

Figure 4.1: Reactor Inlet Pressure(MPa) for 20, 40, 60, and 100% of the RIH area breaks

Figure 4.1 displays the pressure in the broken RIH. Since the pressure at the inlet header at any instance in time is a function of the total inventory lost (with a weak dependence on reactor power, the pump head, and the local flow transients), and the rate of depressurization of the two headers are approximately equal, breaks where the recovered reactor header pressure is close to the ROH pressure lead to the lowest header to header differential pressures. The header to header differential pressure being the deriving force for the flow, the convective cooling capability of the fuel for such breaks can be expected to be greatly degraded. Figure 4.2 displays the header to header differential pressure for the first five seconds of the transient. It was found breaks in the range of 35% to 50% encounter the lowest differential pressures for the longest times, leading to flow stagnation across the broken loop.

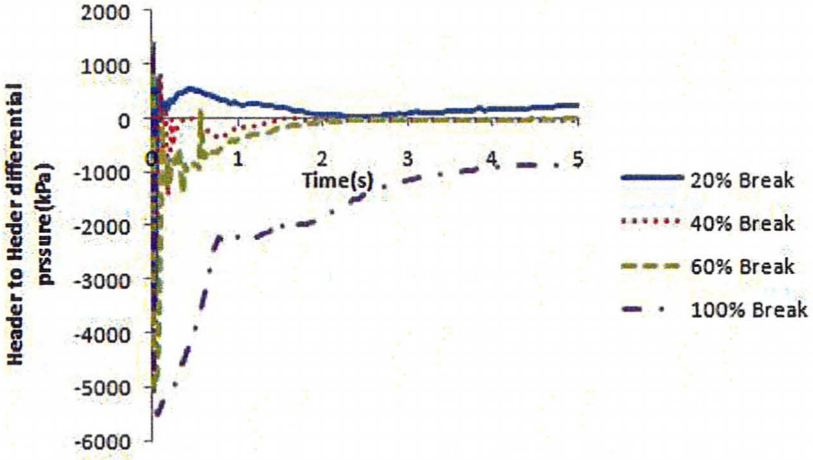

Figure 4.2: Header to Header differential pressure for the first 5s of the transient

For breaks with areas less than 35%, the flow in the loop remains forward, while for breaks with areas larger than 50% flow reversal occurs. For breaks in the range of 35 to 50% of RIH area, flow stagnation occurs as a result of the zero header differential resulting in bidirectional flows across the broken loop. For this range of breaks, the flow in the inlet feeders reverse almost instantaneously while the flow in the outlet feeders remain positive. As a result, for such breaks there is little mass and energy transfer between the two headers in the broken pass. The governing phenomena for such breaks is the buoyancy induced natural circulation resulting from the density gradient across the core. The forces affecting the coolant in the broken loop during this period can be categorized as forces acting to drive the fluid in the normal flow direction and those acting to decelerate the fluid. The driving forces are due to the header differential pressure ΔP and the hydrostatic density gradient caused by the difference between the inlet feeder/channel inlet and outlet feeder/channel outlet $g([\rho\Delta z]_{\text{inlet}} - [\rho\Delta z]_{\text{outlet}})$. The frictional forces F_{fr} act to decelerate the fluid. The flow in the channel is expected to de-accelerate if the total deriving force is less than the frictional forces. The condition for flow stagnation can therefore be represented as:

$$\Delta P + g([\rho \Delta z]_{\text{inlet}} - [\rho \Delta z]_{\text{outlet}}) < F_{fr} \tag{4.1}$$

The header to header differential pressure is driven by the overall heat transport response and is the same for all channels. It is therefore expected that in channels with low powers and low elevations (groups 1 and 2) giving rise to the smallest buoyancy heads, flow stagnation and reversal will occur earlier than in channels with higher elevations (groups 5, 6). This phenomena can be observed in comparing the flows for channels in group 1 through 6 (Figure 4.3.2). It can be seen that due to the lower elevations of the channels, the buoyancy head defined as $H = g([\Delta z \rho]_{\text{inlet feeder}} - [\Delta z \rho]_{\text{outlet feeder}})$ reduces rapidly in regions 1 resulting in flow reversal. An interesting phenomena occurs for channels in groups 3 and 4. In these channels, the initial buoyancy head (dependent on the channel power) dictates the reversal time with flow reversal occurring later in high power channels.

Voiding in the critical pass occurs immediately following the break due to depressurization and boiling enhanced by the power excursion. The Voiding transient for the broken pass is shown in the figure 4.8. Voiding occurs at the channel outlet (point with the highest saturation pressure/highest coolant temperature) and propagates to the channel inlet. Convective heat transfer from the fuel promotes the voiding process so that channels with high power are expected to void earlier than the lower power channels. The positive void reactivity feedback results in a power excursion which is terminated by the shutdown system (SDS1) on either the NOP or the HLR trips. It is assumed that the earlier trip is not functional so that the condition for activation is to chose the later of the two. For breaks in the stagnation region (35 to 50 %), it was found that the high log rate trip is sensed at a later time than the NOP trip due to the larger time constants involved with the instrumentation.

Peak power during the transient is dependent on the effective rate of vapor generation in the broken loop, with the 60% break resulting the highest peak powers. Fuel centerline temperatures increase as a result of the power excursion and deteriorated cooling capabilities due to reduction in flow and voiding. The net energy deposition in the fuel, defined as the total energy added or removed from the fuel over the period of the transient, provides a measure for the energy stored in the fuel during the transient. The fuel heat content at any time is the sum of the initial energy stored in the fuel, and the net energy deposited in the fuel. This quantity is a good measure for expected sheath temperatures as well as possible pressure tube ballooning. The higher the net energy deposition, and the higher the initially stored energy in the fuel, the higher the fuel centerline and sheath temperatures, and the potential for ballooning. The NED is therefore chosen as the figure of merit (FOM) and is evaluated by summing the net energy deposition of all the nodes in the broken core. Figure 4.3 displays the net energy deposited into the fuel at t=5s for break areas of 20 to 100% reactor inlet header flow area in 1% intervals. The critical break, defined as the break with the highest NED at t=5s, was found to occur at the break area of 48% of the reactor inlet header flow area.

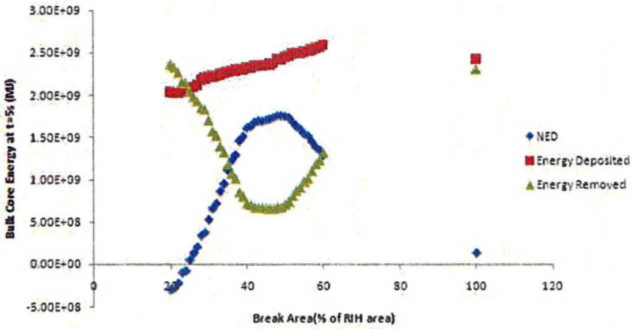

Figure 4.3: NED(MJ) at t=5s for various break sizes in 1% intervals

4.2 Parametric Effect Study

Figure 4.4 displays the static quality at the reactor inlet header. As seen, for the first three seconds of the transient $x = 0$ and the coolant in the RIH is essentially subcooled. Over this period equation 3.46 reduces to[29]:

$$G_c^2 = [(v_{v,eq} - v_{l,0})\frac{N}{(s_{v,eq} - s_{l,eq})}\frac{ds_{l,eq}}{dP}]_t^{-1} \tag{4.2}$$

where $N = 1$ for single phase liquid flow. Since the power pulse phase of the transient is essentially over by t=3s, the thermal nonequilibrium coefficient C_{ne} has little effect on the peak power and NED.

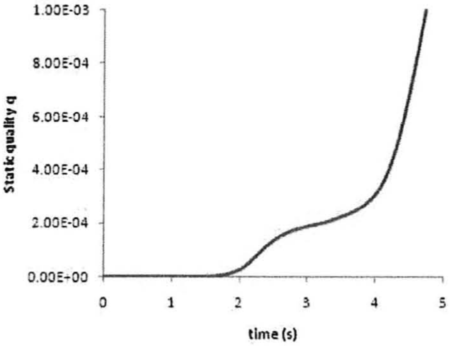

Figure 4.4: Static quality at the inlet header

Figure 4.5 displays the RIH pressure vs. the total inventory lost (defined as $\int W_{\text{break}}dt$) for the reference case, and for constant reactor power (no feedback). As seen, the RIH pressure is a function of the total inventory lost and is only weakly dependent on the reactor power (and the pump head). The mass flux G at any instance in time is calculated as $G = C_{\text{discharge}} * G_c$ where G_c is computed from equation 3.46 and $C_{\text{discharge}}$ is the orifice discharge coefficient discussed in chapter 3. Increasing the discharge coefficient will therefore have the effect of increasing the inventory lost as a function of time (figure 4.6) leading to a more rapid depressurization rate(figure 4.7), while

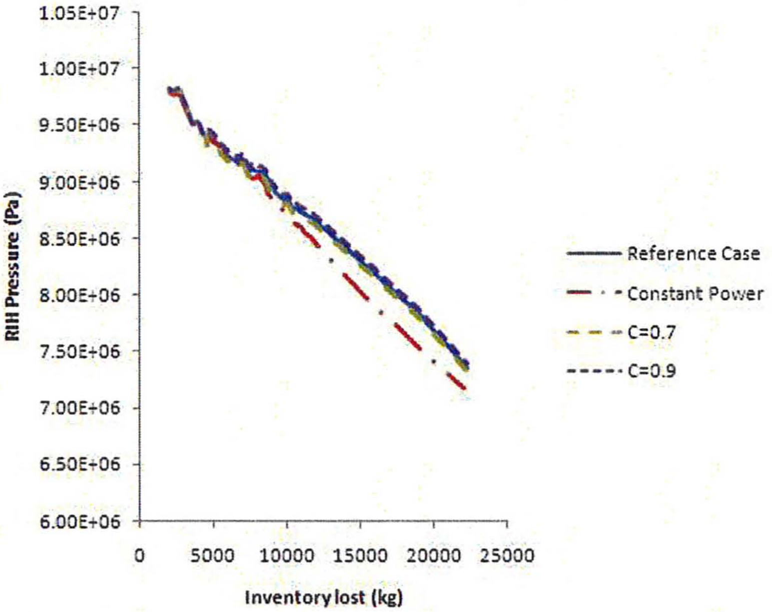

Figure 4.5: RIH Pressure(Pa) vs. total inventory lost (kg)

decreasing the discharge coefficient $C_{\text{discharge}}$ has the opposite effect leading to a less rapid depressurization. Subsequently, voiding in the core due to depressurization (flashing) will be enhanced for higher discharge coefficients leading to higher peak powers.

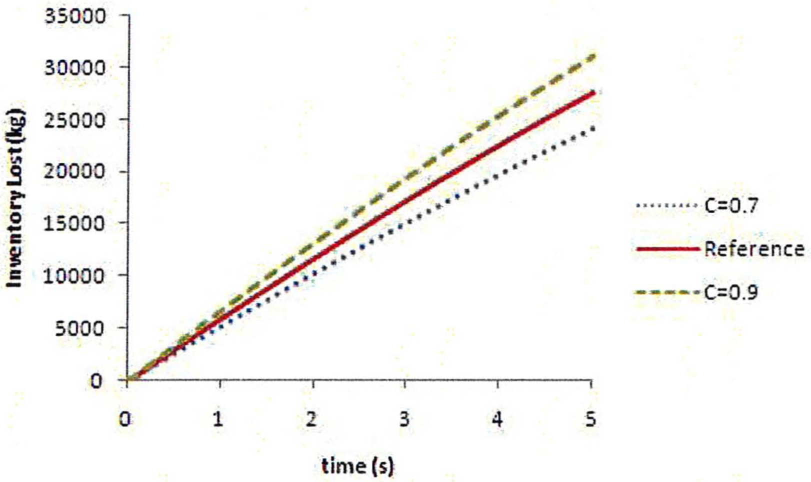

Figure 4.6: Inventory lost (kg) vs. time

Due to the depressurization of the HTS, the coolant in the broken pass reaches saturation conditions almost immediately following the break and the effect of single phase heat transfer is minimal. Lower single phase heat transfer coefficients result in higher initial sheath temperatures while higher single phase heat transfer coefficients result in lower initial sheath temperatures.

Figure 4.8 displays the average core void and its derivative with respect to time quantifying the voiding rate. Due to local fluctuations, the derivative has been calculated from the average core void defined as $\bar{\alpha}_{\text{core}}(t_i) = \frac{\int_{t_i}^{t_i+\Delta t} \alpha_{\text{core}}(t)dt}{\Delta t}$ for $\Delta t = 10\text{ms}$ intervals. As displayed, there is a steady increase in the voiding rate until CHF is reached(usually at node 10 or 11). Upon reaching CHF, the liquid is no longer in contact with the wall and little voiding takes place leading to a rapid reduction in the void generation rate. Due to the lower pressures and higher coolant internal energies at the channel outlet, CHF is reached near the channel exit and propagates upstream. Figure 4.9 displays the local vapor generation rate in the average channel of the broken pass at bundles 12, 7, and 1. Note that the coolant at the channel exit reaches saturation conditions immediately following the break.

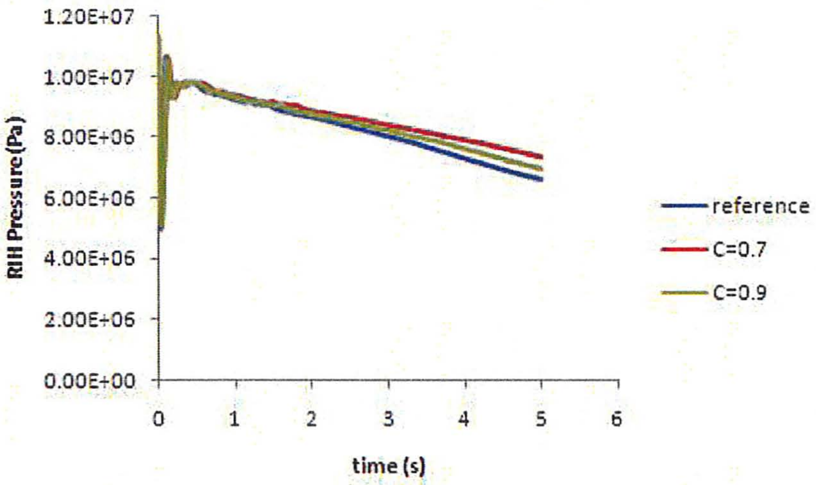

Figure 4.7: Inventory lost (kg) vs. time

Prior to reaching CHF, the heat transfer coefficient is calculated from equation 3.37. Boiling enhanced voiding is dependent on the wall superheat with lower wall temperatures leading to lower voiding rates. It can therefore be expected that increasing the pre-chf heat transfer coefficient has the effect of decreasing the voiding rate across the core and thereby resulting in lower peak powers while decreasing the heat transfer coefficient has the effect of increasing the wall superheat and thereby increasing the voiding rate resulting in higher peak powers. Simultaneously, higher heat transfer coefficients naturally result in greater energy removals and lower NEDs. Figure 4.10 displays the core average void during the first 0.6 seconds following the break for pre-chf heat transfer coefficient multipliers of 0.9 and 1.1. Higher CHF values result in longer liquid-sheath contact times and thereby higher voiding times and consequentially slightly higher peak powers. As reactor power is rapidly increasing in this phase, the new CHF value is reached with little delay so that this effect is fairly negligible.

Post dryout heat transfer has a direct effect on the energy removal rate with higher post dryout heat transfer coefficients resulting in lower NEDs. Due to the low heat

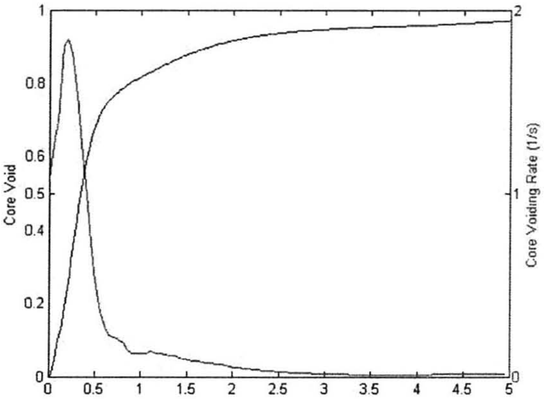

Figure 4.8: Average core void in the broken pass (blue line) along with the voiding rate (green)

transfer coefficients involved in this phase of the transient, variations in the PDO heat transfer coefficient have little impact on results.

Uncertainties for the fuel thermal conductivity k and heat capacity c_p were discussed in chapter 3. The heat conduction equation has the form:

$$\rho c_p(T,\bar{x})\frac{\partial T(\bar{x},t)}{\partial t} - S = \nabla\cdot(k(T,\bar{x})\nabla T(\bar{x},t)) \tag{4.3}$$

Under steady state, the first term is zero and the flux term equates the source. It is easy to show that the dominating terms in the the steady state solution $\gamma(\bar{x},k)$ are inversely proportional to the thermal conductivity k. If one were to assume that the transient solution is of the form $T(t,\bar{x}) = \eta(t,\bar{x})\gamma(\bar{x},k)$ (i.e. the fuel heat up rate is independent of k), then perturbations of γ from variations in k of the form $k = \alpha k_0$ can be approximated as $\gamma = \frac{1}{\alpha}\gamma_0$ where γ_0 is the steady state solution for $k = k_0(T)$. Figure 4.12 displays the steady state radial temperature distribution of the outer ring elements of bundle 7 for the average channel in the reference case, as well as for $\alpha = 1.04$ and $\alpha = 0.96$ along with the steady state solution for the reference case $\gamma_0(r)$ and $\frac{\gamma_0(r)}{\alpha}$ for the mentioned α's. The validity assumption of the independence

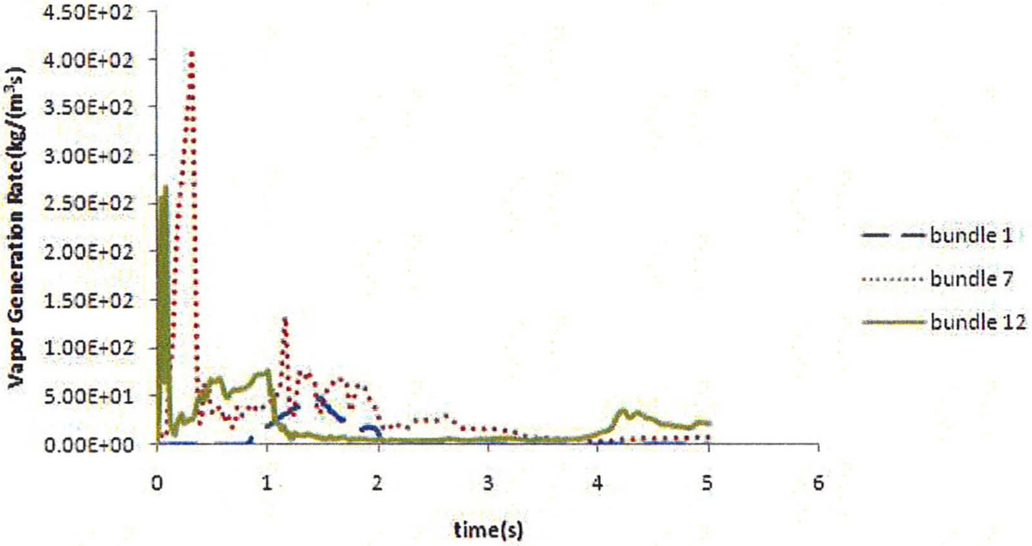

Figure 4.9: Propagation of CHF upstream of the channel exit and its effect on vapor generation

of the heat up rate on the thermal conductivity can be seen in figure 4.12.

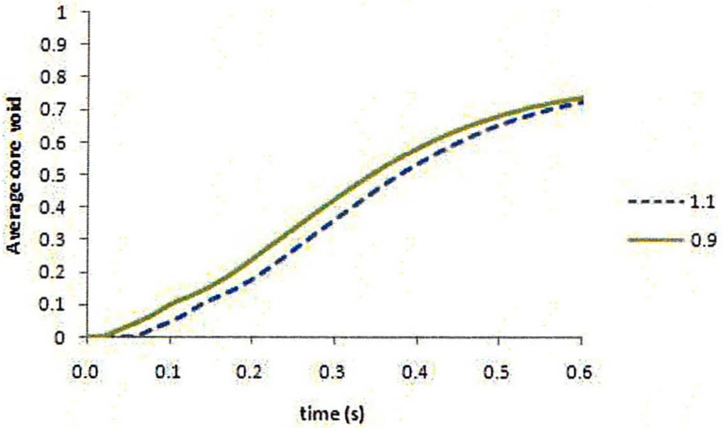

Figure 4.10: Void in the core for nucleate boiling multipliers 0.9 and 1.1

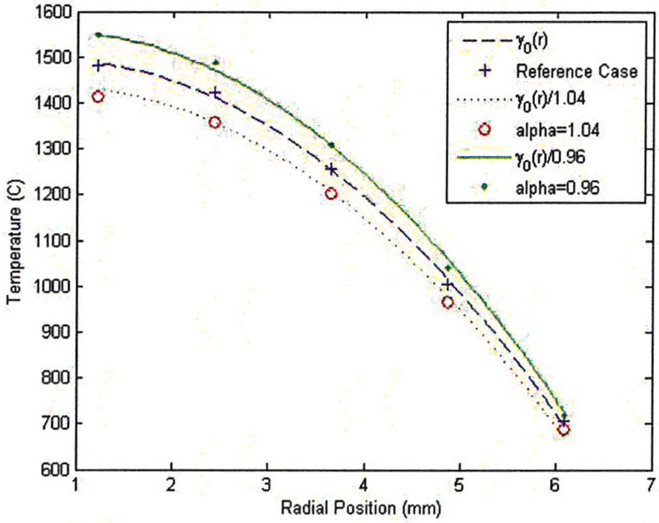

Figure 4.11: Effect of the thermal conductance on the steady state temperature distribution function $\gamma(r)$ for the outer elements of the average channel

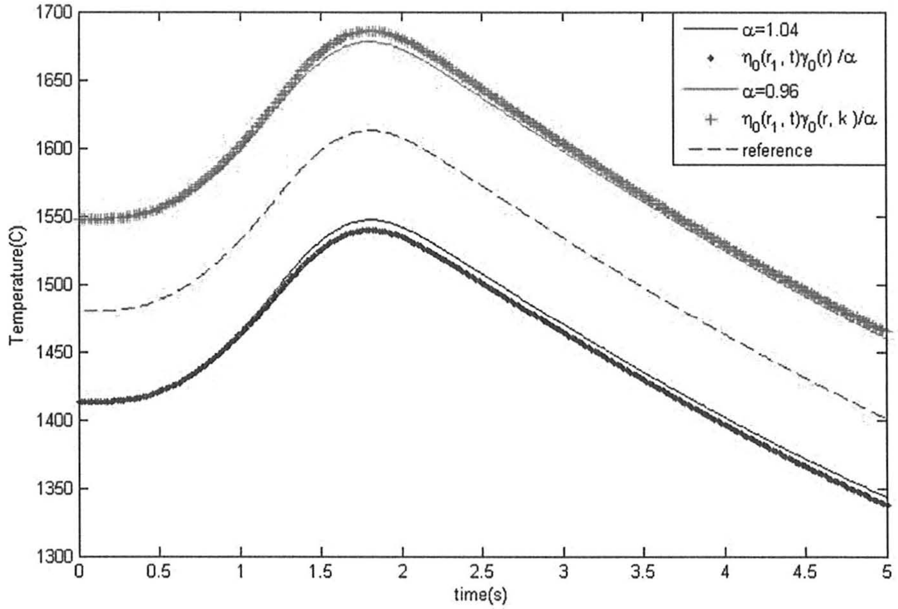

Figure 4.12: Temperature profile for the outer elements of the average channel at r=1.22mm exhibiting the independence of the heat up rate on k

The uncertainty for the fuel heat capacity c_p was reported as 3% in chapter 3. The uncertainty in the density is reported as 0.18 $\mathrm{Mg/m^3}$ which is approximately equal to 0.1% and can therefore be considered as negligible so that the uncertainty for the volumetric heat capacity $C = \rho c_p$ is assumed to be 3%. To quantify the effect of the uncertainty in the volumetric heat capacity, let $C \to C_0 + \alpha C_0$ and the resulting perturbation on $T \to T_0 + \eta(t)$. Since the volumetric heat capacity only affects the fuel heat up rate, it is reasonable to assume that η is independent of spacial coordinates. Substitution of the new temperature profile into equation 4.3, and assuming that the source term S is not affected by the perturbation(fuel temperature feedback is negligible) yields $\frac{\partial \eta}{\partial t} = -\alpha \frac{\partial T}{\partial t}$ so that the heat up rate is given as:

$$\frac{\partial T}{\partial t} = (1-\alpha)\frac{\partial T_0}{\partial t} \tag{4.4}$$

The fuel is therefore expected to heat up faster for negative α (lower heat capacities) and slower for positive α. Figure 4.12 displays the fuel heat up rate $\frac{\partial T}{\partial t}$ for $\alpha = 0.97$ and $\alpha = 1.03$ for bundle 7 in the average channel channel along with the calculated profile from equation 4.4.

Variations in the void reactivity coefficient have a great effect on the power profile with larger void reactivity coefficients leading to higher peak powers and NEDs. Increasing the delayed neutron fraction results in the reactor operating on fewer prompt neutrons, resulting in a slower response time and lower peak powers. Similarly, decreasing the prompt neutron lifetime results in faster response times quantified as a more rapid power excursion and higher peak powers. Decreasing the net worth of SDS1 results in a less rapid reactivity decay and hence larger peak powers and a slower decay of reactor power to that of the decay heat. Similarly, NOP detector time constants or HLR trip delay mean later activation of the shutdown system resulting in higher peak powers and NEDs.

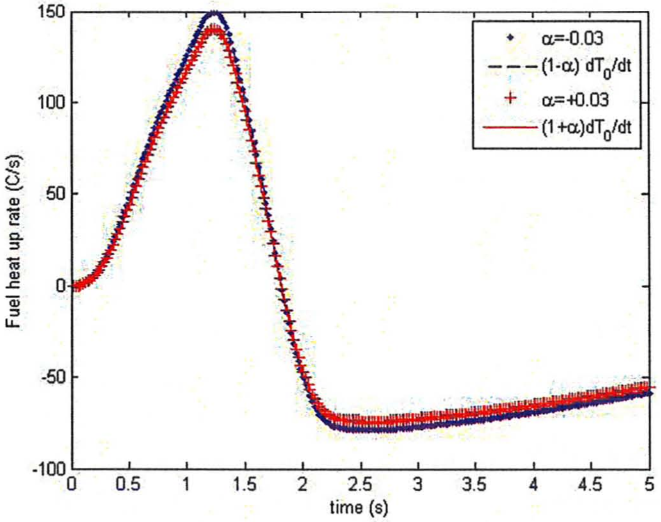

Figure 4.13: Fuel heat up rate $\frac{\partial T}{\partial t}$ for $r = 1.22\text{mm}$ for $\alpha = \pm 0.03$

Table 4.1 summarizes the results of this section. Best Estimate values for the considered parameters along with their uncertainties are listed in table 4.2 and will be used in the sensitivity analysis section. Trip set points are assumed to be bounding. In quantifying the uncertainties for the time constants, uniform distributions were assumed with a 40% width.

Bulk Power	Peak Power and bulk net energy deposition
ROH Pressure	Coolant voiding rate
RIH Temperature	Coolant voiding rate
Break Discharge Coefficient	Coolant voiding rate
Pre-CHF heat transfer coefficient	Coolant voiding rate net energy removal
CHF multiplier	Coolant voiding rate
Post-Dryout heat transfer	Net energy removal
UO_2 thermal conductivity	Maximum fuel centerline temperature
UO_2 heat capacity	Fuel heat up rate
RIH/ROH pressure differential transient	Blow down cooling
Prompt neutron lifetime	Power pulse and bulk net energy deposition
Delayed neutron fraction	Power pulse and bulk net energy deposition
Coolant void reactivity coefficient	Power pulse and bulk net energy deposition
Fuel temperature reactivity feedback coefficient	Power pulse and bulk energy deposition
SOR reactivity worth	Power pulse and bulk net energy deposition
SOR insertion timing gates	Power pulse and bulk net energy deposition
HLR trip delay	Power Pulse and bulk net energy deposition

Table 4.1: Key parameters and their affecting phenomena

Parameter	Type	BE value	σ
Bulk power (% FP)	ND	101.5	0.018
ROH Pressure (MPa)	ND	9.8 MPa	0.019
RIH Temperature (° C)	ND	265	0.17
Break Discharge Coefficient	ND	0.8	0.109
Pre CHF HTC	ND	1.0	0.154
CHF Multiplier	ND	1.5	0.16
Post Dryout HTC	ND	1.0	0.20
UO_2 thermal conductivity	ND	1.0	0.043
UO_2 specific heat	ND	1.0	0.03
Λ (s)	ND	9.02e-4	0.05
β_{eff}	ND	0.00582	0.0046
Void Reactivity Coefficient (mk)	ND	15.8	0.12
Fuel temp reactivity (mk)	ND	-	2 mk
SOR worth (mk)	ND	-62.3	0.05
SOR timing gates	UD	1.0	0.02
NOP trip setpoint	-	1.2	
NOP time constant (ms)	UD	100	0.4 ms
HLR trip setpoint	-	1.10	
HLR trip delay(ms)	UD	120.0	0.4

Table 4.2: Statistics for Parameters.

ND:Normal Distribution, UD:Uniform Distribution

σ: Standard deviation or distribution width

4.3 Nodalization Study

4.3.1 Channel Nodalization

To study the physical convergence and accuracy of the RELAP5 model, the nodalization of the channel was analyzed. Three nodalization schemes were considered with the channel having 6, 12 and 24 nodes. The latter two cases were identical and will not be considered. Comparisons between channel local pressures, voiding rates, and densities were made by interpolating the 6 node results using a 5th order polynomial. the polynomial curve passes through the original six points of the 6 node model. The domain axis is divided into 12 sections and the x-values are substituted into the polynomial to obtain the 12 node interpolated results. The results show little variations in that the two models are in good agreements. As a result of the coarseness of the nodalization, centerline fuel temperatures for the average channel were estimated at a lower temperatures (no more than $2^{c}irc$C) for the five node representation.

4.3.2 Core Modeling

The validity of the single group modeling of the critical pass lies in the assumption of thermal hydraulic similarity between all channels in the broken loop. Therefore, while a single channel model may accurately predict the total flow across the core, this flow is not representative of the local channel flows and may under/over estimate the local voiding rate and fuel cooling rate. A six group representation of the core has therefore been considered. Table 4.3 displays the feeder properties for each channel group. The results show that the single channel model tends to slightly predict faster voiding than the multi channel model resulting in a slightly higher power.The reasoning for this can be found by comparing the voiding rate for the channel groups. Channel groups with the highest power (channels 3 and 4), tend to reach CHF quite early, after which voiding essentially stops. The effect of local channel flows can be measured by the net energy deposited in the fuel. Figure 4.18 shows that less net energy(at t=5s) is predicted to be deposited in the core using the multi channel core pass representation when compared to the single channel representations. Aside from the slightly lower powers predicted for the multi-pass representation, the discrepancy in the NED is due to the under prediction of the buoyant force in the early phase of the transient resulting in flow reversal accompanied with degraded cooling capabilities occurring earlier.

In general, while the overall HTS response is independent of the particular channel representation, local effects such as voiding, channel flows, and fuel temperatures in individual channels cannot be predicted accurately using the single channel group model.

Group	Feeder	Length(m)	Area(m^2)	Δz(m)	K(Pa/Pa)	HD (m)
1	Inlet	9.90	0.0337	-5.24	1.058	0.0426
1	Outlet	13.35	0.0482	+5.62	0.845	0.0518
2	Inlet	11.35	0.0572	-6.22	1.155	0.0470
2	Outlet	14.81	0.0787	+6.59	0.572	0.0578
3	Inlet	11.25	0.0635	-6.20	1.206	0.0544
3	Outlet	14.62	0.0872	+6.57	0.561	0.0525
4	Inlet	16.01	0.0713	-8.18	1.229	0.0547
4	Outlet	19.50	0.0968	+8.55	0.446	0.0525
5	Inlet	17.27	0.0629	-9.04	0.891	0.0535
5	Outlet	20.81	0.0865	+9.42	0.383	0.0598
6	Inlet	17.52	0.0326	-9.64	0.614	0.0423
6	Outlet	21.06	0.0521	10.01	0.826	0.0523

Table 4.3: Feeder properties

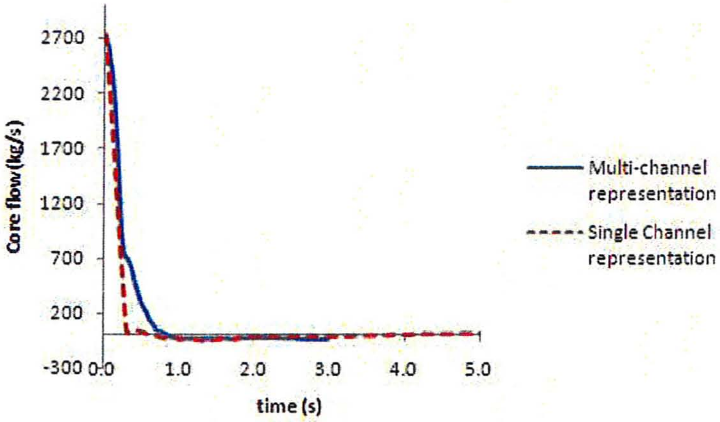

Figure 4.14: Total core flow for the multi grouped and single group models

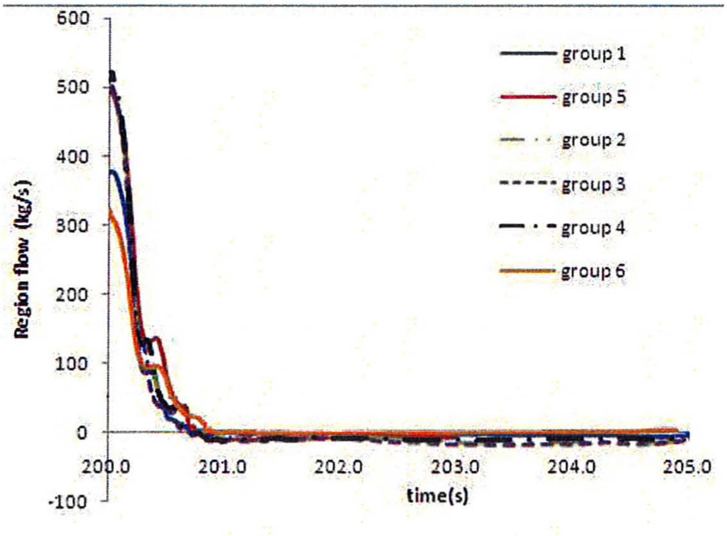

Figure 4.15: Region specific channel flows

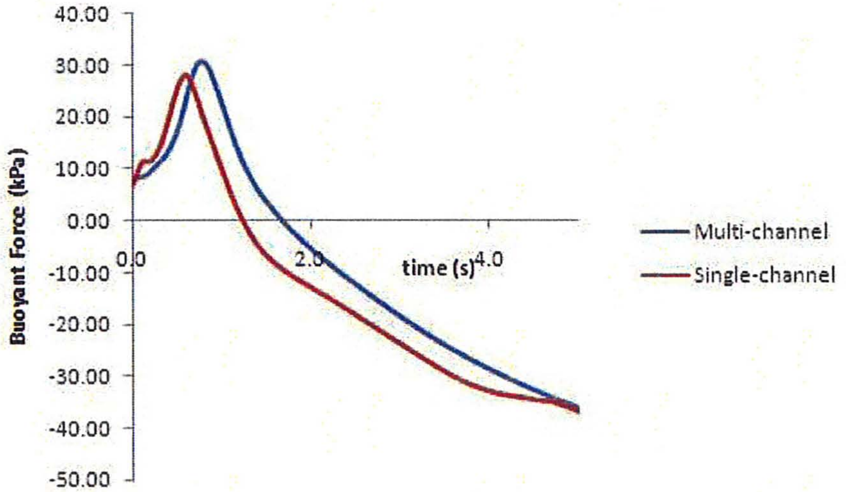

Figure 4.16: Total buoyant force for the multi grouped and single group models

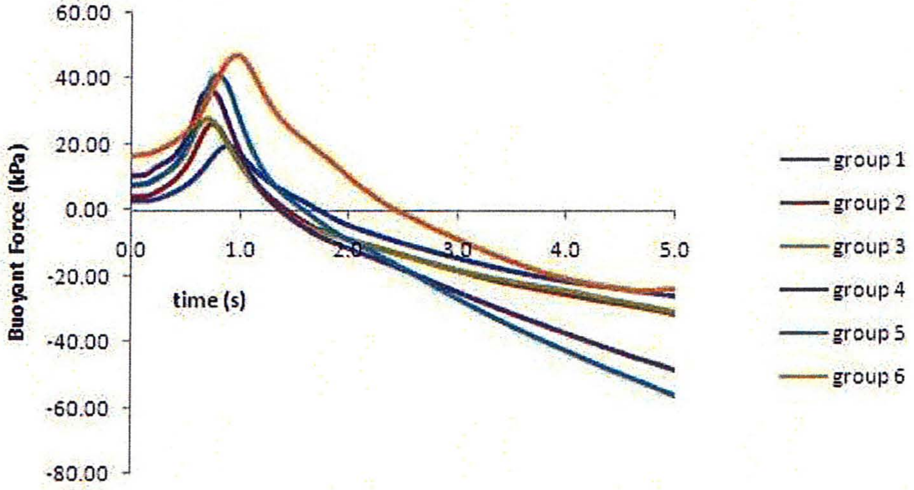

Figure 4.17: Regional buoyant force (kPa)

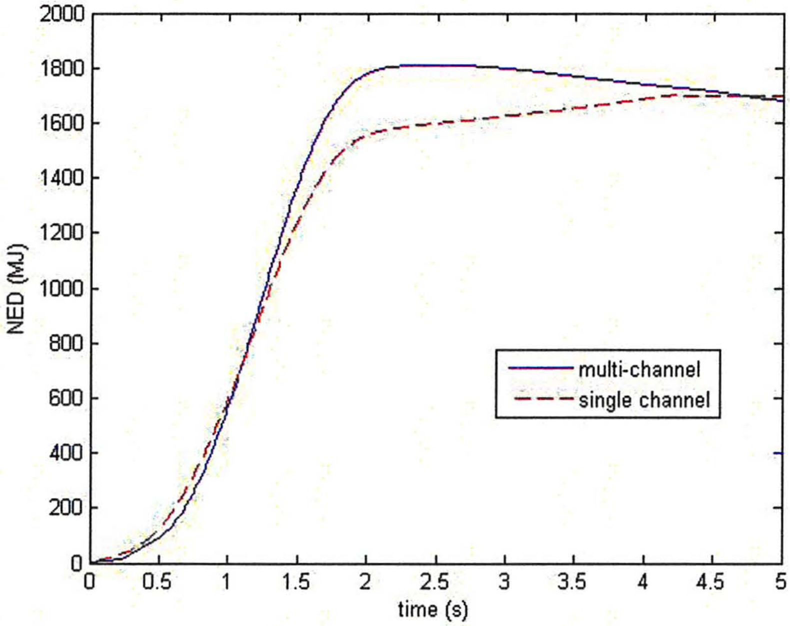

Figure 4.18: Total core NED for the single group and multi group models

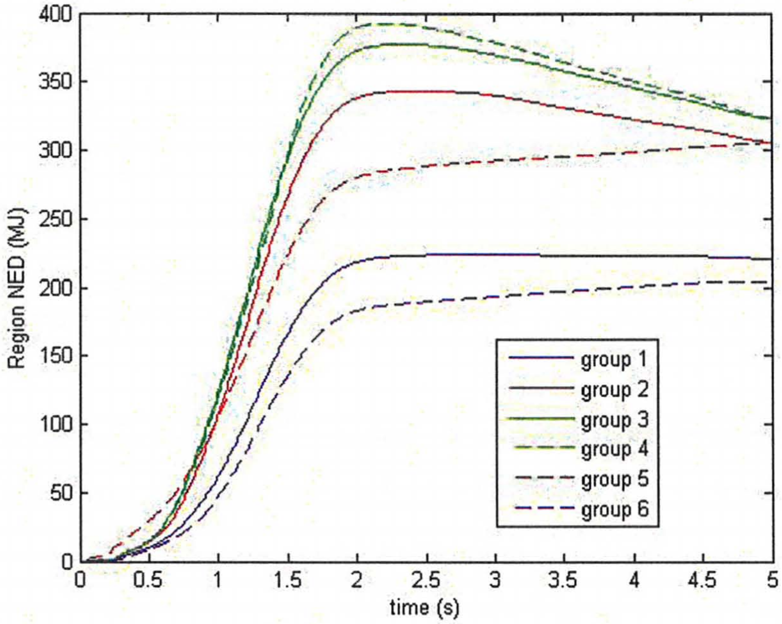

Figure 4.19: NED in various core regions

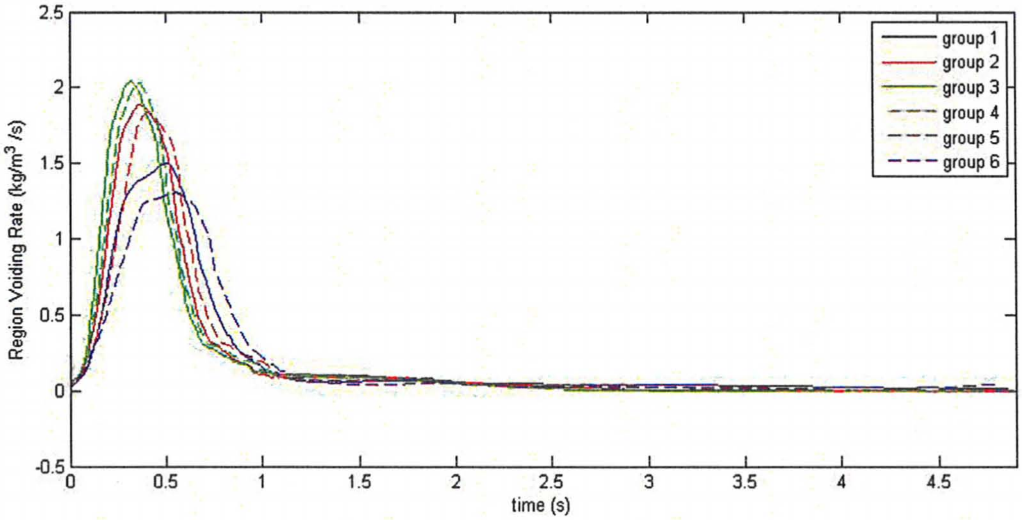

Figure 4.20: Void generation rate in various core regions

4.3.3 End Fitting Discharge

Figure 11.5 of reference [38] displays a 37 rod fuel bundle CANDU end fitting. As seen, the end fitting can be decomposed into three regions. The coolant enters from the inlet feeders to the inlet end fitting through the gray lock connection, and flows along the annulus section between the liner outer diameter, and the end fitting body to the common volume section where it enters the channel. A stagnant D_2O section resides at the back of the shield plug accounting for approximately 50% of the end fitting total volume. Under normal steady state conditions, the coolant in this section is stagnant and does not contribute to the overall flow. In reference [20], the end fitting is modeled with the effective flow length and area of the annular and the common volume sections, accounting for the stagnant D_2O volume by inputting the total volume of the end-fitting (used by the code to calculate the available coolant inventory of the module). As a consequence of the one node approach, the coolant in the stagnant section is assumed to discharge at the same time as the common volume area resulting in a faster depletion of the end fitting total coolant inventory. The impact of this assumption on the cooling capability of the channel is examined in this section.

A more detailed model of the end fitting has been constructed, using three separate components to model each of the end fitting regions. The pressure loss is divided equally amongst the annulus and common volume sections, with the nodalization represented in the figure 4.21. Following the break, the flow from the stagnant volume is dependent upon the local pressure transients in the end fitting volume with

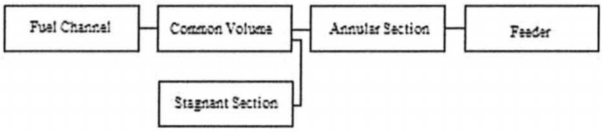

Figure 4.21: 3-component nodalization of the End fitting

coolant discharged from the stagnant section once pressure in the common volume section falls below that in the stagnant section. As a result of the earlier voiding and the higher enthalpy of the coolant in the outer end fitting (channel outlet), depressurization usually occurs earlier in the outer end fitting(OEF) than the inlet end fitting(IEF) with the coolant in the stagnant section discharging at an earlier time from the OEF(figure 4.22). The discharged coolant is in the same direction as the feeder flows.

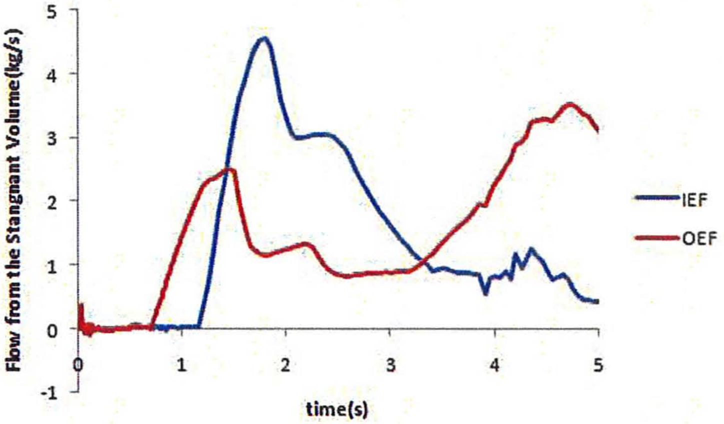

Figure 4.22: Discharge(kg/s) from the stagnant D_2O section for the inlet and outlet endfittings for the average channel

For high elevation channels in groups 5 and 6, and high power channels in groups 3 and 4 flow reversal takes place quite later(at t=1.5s) as a result of the maintained and relatively high buoyancy head and the discharged coolant is in the normal flow direction. Therefore, the coolant is discharged from the outlet end fitting to the outlet feeders contributing to cooling the outlet feeders in these channels. For the lower elevation channels and the lower power channels, where flow reversal takes place early, the coolant from the end fitting is discharged into the fuel channels and assists in cooling the fuel rods during early blow down.

The discharge from the inlet end fitting is similar. Since the inlet feeders reverse flow directions almost instantaneously following the break, the coolant discharged from the inlet end fitting contributes to cooling the inlet feeders during the power pulse phase of the transient, particularly for low power and low elevation channels in which flow reversal is prolonged during the power pulse phase of the transient.

Since low power channels and low elevation channels which experience early flow reversal have the advantage of additional coolant entering the fuel channel from the outer end-fitting following coolant discharge from the stagnant D_2O section at $t \approx 0.75$s, overall cooling of the core is improved with the three component model. This effect on NED is not very large but may be seen by comparing the NED over the first five seconds of the transient. The 3 node model of the end fitting results in a lower NED, estimated by approximately $\Delta NED = \int h_{fg}\dot{W}_{OEF}dt$.

4.4 Sensitivity Analysis

In order to reduce the number of important parameters to be considered in the integrated uncertainty analysis, sensitivity analysis must be performed. The phenomena and key parameter identification table (PKPIRT) provided in reference [45] will be used as the initial PKPIRT. Parameters not deemed to have a high sensitivity will be excluded from the PKPIRT. The local sensitivity of a variable provides a measure of the change in the FOM, resulting from a corresponding change in the parameter. As suggested in reference [45], a number of values $\{x\}$ will be taken for each variable lying within one standard deviation of the best estimate point. A least square linear regression is then performed to estimate the linear contribution of the sensitivity to the FOM. The regression is performed with the FOM as the dependent variable. The sensitivity S is defined as the slope of the regression line(figure 4.23) and provides an estimate for the directional derivative of the figure the FOM surface with respect to the parameter x.

In order to ensure that the local sensitivity calculated near the best estimate point x_{be} provides an accurate representation of the local sensitivity over the 2σ interval, similar calculations of the sensitivity are also performed at the non best estimate point $x_{nbe_{1,2}} = x_{be} \pm \sigma$. Using x_{nbe} as the center, the local sensitivity is calculated using the methodology described above.

The sign of the sensitivity is dependent on the nature of the parameter considered. The rank of each parameter is calculated as $r = \sigma * \max(|s_i|)$ where s_i is the sensitivity normalized to the center point and the max function refers to the maximum of the relative sensitivity at the three considered center points $\{x_{be}, x_{nbe_1}, x_{nbe_2}\}$. The Pearson coefficient r_p defined in chapter 3 is used to evaluate wether the sensitivity defers statistically from zero. Those parameters with a low Pearson coefficient ($r_p \leq 0.2$) will be assumed as having no correlation with the FOM (the slope is statistically zero) and are ranked as low, regardless of the magnitude of the calculated sensitivity. A parameter x_i is ranked relative to the other parameters such that:

$\alpha_i \geq 0.5$	ranked as having high importance (H)
$0.5 > \alpha_i \geq 0.2$	ranked as having medium importance (M)
$0.2 > \alpha_i$	ranked as having low importance (L)

where $\alpha_i = \frac{r_i}{\max_{j \in PKPIRT}(r_j)}$. Tables 4.5 and 4.6 display the calculated sensitivities and their respective ranks displayed in table 4.7.

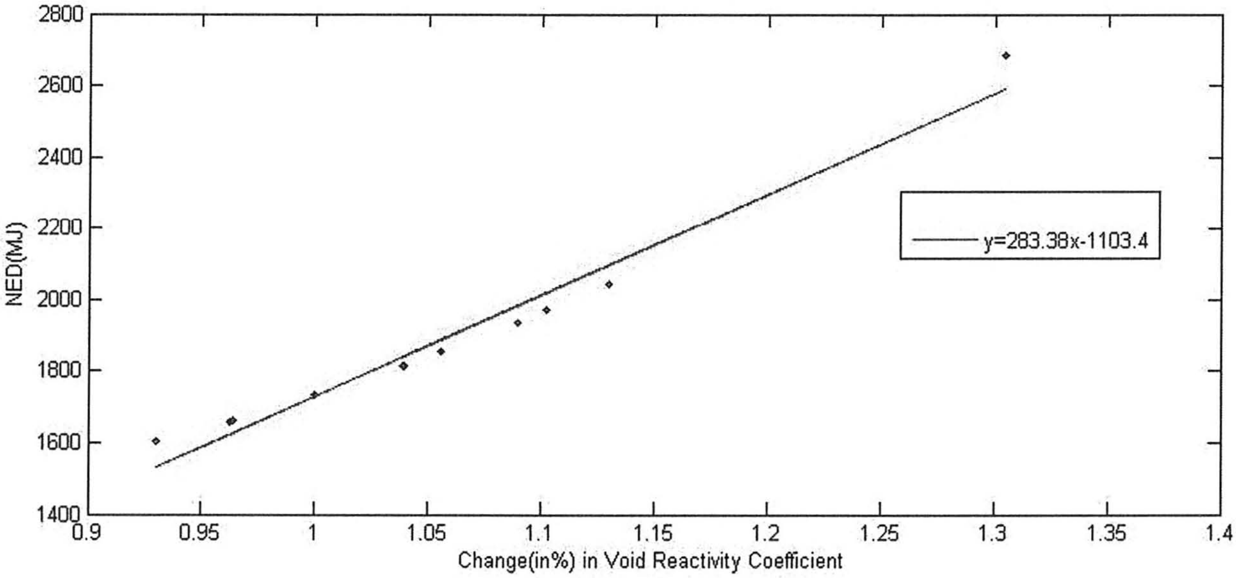

Figure 4.23: Variation of the NED (MJ) with respect to Void Reactivity Error Allowance

Parameter	Sensitivity S(J/%)	normalized slope (s)	$s * \sigma$	p-value
Void Reactivity	2.83E9	1.6357	0.2071	0.9851
NOP trip delay	7.05E8	0.40634	0.162536	0.9991
HLR trip delay	6.88E8	0.3975	0.1590	0.9992
Break discharge	5.38e9	0.3658	0.1142	0.978
Post-dryout HTC	-3.46E7	-2.00E-03	4.00E-02	0.9661
Bulk Power	3.19E9	1.8387	0.0331	0.9971
β	-1.12E+9	-0.6438	0.0297	0.9965
ROH Pressure	-2.44E9	-1.4059	0.0239	0.9982
SOR worth	-6.65E8	-0.3839	0.0192	0.9996
CHF multiplier	1.49E8	0.0859	0.0137	0.9809
Pre-chf HTC	-8.20E7	-0.0474	0.0073	0.9891
Temperature feedback	-3.12E8	-6.41E-01	-3.8E-02	0.9994
Λ	-1.27E8	-0.0731	0.0037	0.9969
k_{fuel}	-8.12E7	-0.0468	2.00E-03	0.9994
Channel losses	-1.01E7	-0.0059	5.85E-04	0.5216
Fuel C_p	4.56E+5	2.63E-4	7.90E-06	0.1699
Feeder losses	1.98E+5	0.00011443	5.72152E-06	0.5513

Table 4.5: Calculated sensitivities with the NED as the FOM

Parameter	Sensitivity S(Watts/%)	normalized slope (s)	$s * \sigma$	p-value
Void Reactivity	3.11E9	0.4503	0.057	0.9840
β	-6.11E9	-0.8842	0.0409	0.9977
break discharge	1.90E9	3.05E-01	3.33E-2	0.986
NOP trip delay	8.28E8	0.1199	0.0192	0.9899
CHF	8.28E8	1.20E-1	1.92E-02	0.9899
Bulk Power	9.61E9	1.54E+00	1.85E-2	0.9995
ROH Pressure	-4.73E9	-0.684	1.16E-2	0.9906
HLR trip delay	1.17E9	0.1876	0.0094	0.9991
Λ	-3.00E9	0.1876	0.0094	0.9985
temperature feedback	-2.43E9	-0.1456	0.0085	0.5934
SOR worth	-6.96E6	-1.01E-01	5.00E-3	0.9988
Pre-chf htc	-1.84E8	-0.267	0.0041	0.8354
k_{fuel}	1.15E8	1.66E-2	7.42E-4	0.9976
channel losses	-4.16E+7	-0.006	6.02E-4	0.6563
feeder losses	-3.15E+7	-0.003	3.03E-4	0.5423
Fuel C_p	-4.67E+6	-6.75E-04	2.03E-5	0.4572
post-dryout htc	4.05E+5	5.86E-05	9.38E-6	0.9908

Table 4.6: Calculated sensitivities with Peak Power as the FOM

Parameter	Rank
Void Reactivity	H
NOP trip delay	H
HLR trip delay	H
break discharge	H
Bulk Power	H
β	M
ROH Pressure	M
SOR worth	M
CHF	M
Λ	M
Temperature feedback	M
Pre-CHF HTC	M
k_{fuel}	M
Channel losses	L
Post-dryout HTC	L
C_p fuel	L
Feeder losses	L

Table 4.7: Parameter Ranking table

H:high, M:Medium, L:Low

4.5 Integrated Uncertainty Analysis

Random numbers are generated for each parameter from the random sampling of the input distributions used in the Monte-Carlo method. In order to ensure that the Monte-Carlo sampling is performed accurately over the entire division range, the Latin Hypercube Sampling (LHS) function (available in Matlab) is used to generate uniform random numbers. A total of 18 intervals are used with 5 intervals used for the bottom 10% of the distribution, 5 intervals used for the top 10% of the distribution, and 8 intervals used for the middle 80% of the distribution. The use of smaller subdivisions in the bottom and top 10 percentiles optimizes convergence in the tails of the sample distribution. Random selection from populations with a cumulative distribution function $F(x)$ are chosen according to[54]:

$$x_n = F^{-1}[R_n] \tag{4.5}$$

where $R_n \in U(0, 1)$ is generated uniformly along the interval (0, 1). In the present work, all distributions are approximated as either normal or uniform.

A total of 10,000 simulations were performed. Each simulation approximately took between 15-20 minutes on an Intel Core 2.4 GHz with the entire execution time for the 10,000 simulations running to about two weeks (using five stations). For each set of input parameters, a steady state solution is established. A test is performed to ensure that the steady state solution conforms to the plant physical readings provided from Darlington Unit 1. Total core flow, and RIH pressures are compared against plant data. The uncertainty of the flow is taken to be at 5% and the uncertainty at the RIH pressure is assumed to be of the same magnitude as that of the ROH pressure. Output for runs that fail this test (or fail to run) are set to three standard deviations from the best estimate value. Results for the Monte-Carlo simulations are displayed in figures 4.26 and 4.27 for the net energy deposited in the broken pass and the reactor Peak Power.

The application of a finite subset to the approximate the statistics of an infinite sample space containing it, with the random nature of the Monte-Carlo method used in its generation result in slightly different values of the 95^{th} percentile for multiple runs. The 95% confidence limit of the 95% percentile may calculated from:

$$p = 95 + 1.645\sqrt{\frac{95 * 5}{10,000}} \tag{4.6}$$

Note that the above value can be applied to any distribution(not necessarily normal). For 10,000 simulations, the 95^{th} percentile with a 95% confidence limit corresponds to calculation of $p = 95.359$.

The Limit of Operating Envelope (LOE) is calculated by placing each parameter at 2σ of its best estimate value in the direction resulting in a positive change in the FOM. Comparisons between the LOE and the 95% quantify the conservative nature of this approach.

The GRS method based on wilk's formula and ordered statistics discussed has also been implemented(figures 4.24 and 4.25). Comparisons between the three methods are displayed in table 4.8. In addition, a comparison between the first order and second order GRS methods is performed. The outputs from the Monte-Carlo simulation are used for the analysis. A distribution for the first order 95/95 GRS predictions is obtained by dividing the 10000 Monte-Carlo runs into (10000/59) groups of 59. Dividing the 10,000 Monte-Carlo runs into (10000/93) groups of 93 and taking the second largest number in the list gives the second order GRS predictions. The cumulative distribution functions for the two methods are plotted in figure 4.28.

	MC 50^{th} percentile	MC 95^{th} percentile	GRS (95/95)	LOE
NED (MJ)	1.79e+003	2.13e+003	2.2507e+003	3.44e+003
Peak Power (% of FP at BE)	2.4124	2.9349	3.011	4.6784

Table 4.8: Comparison of the Monte-Carlo (MC), GRS, and LOE methods for NED (MJ) and Peak Power (% of 2690 MJ)

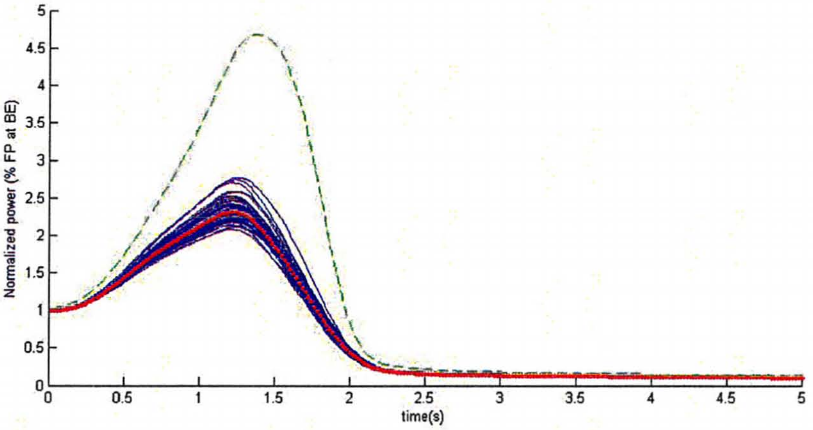

Figure 4.24: Power trajectories for the 59 GRS runs along with the reference case(red) and the LOE case(green)

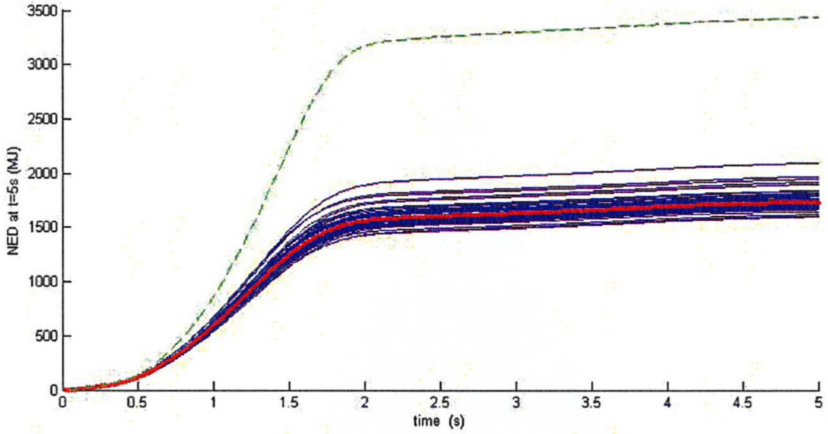

Figure 4.25: NED trajectories for the 59 GRS runs along with the reference case(red) and the LOE case(green)

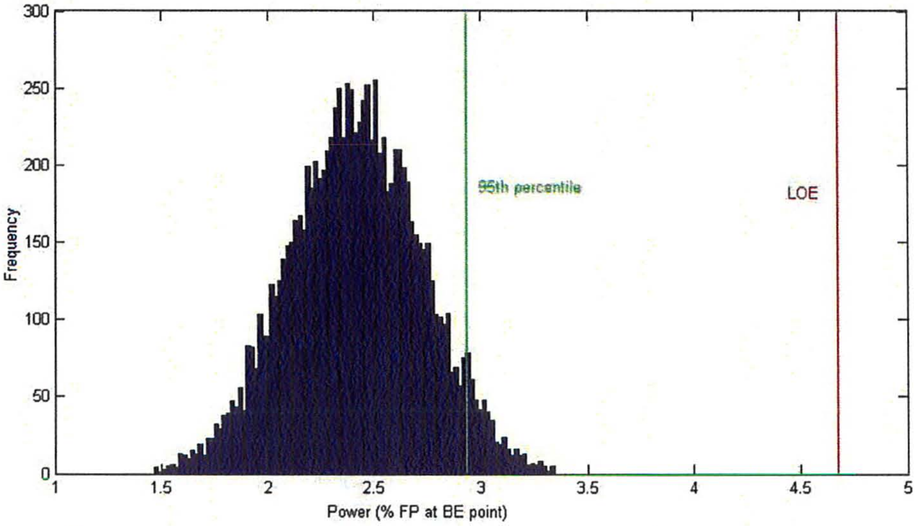

Figure 4.26: Peak Power(% FP) probability distribution

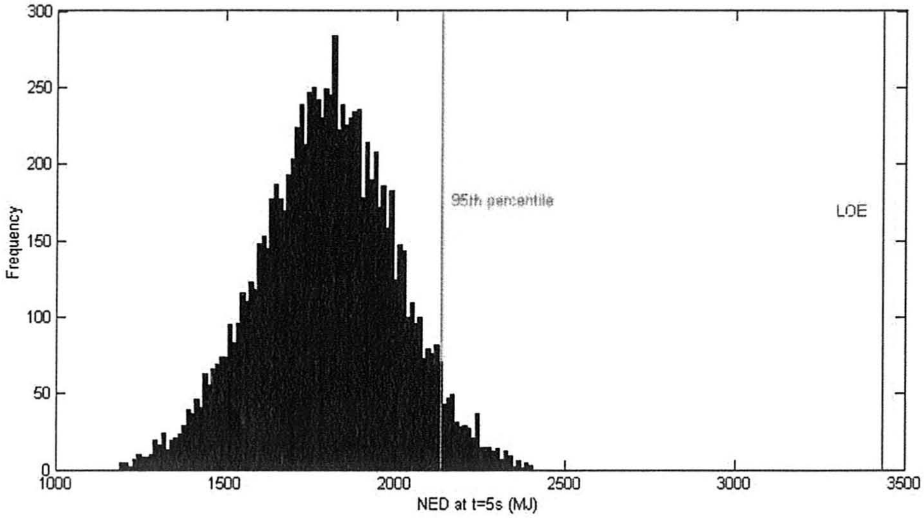

Figure 4.27: Bulk NED(J) probability distribution

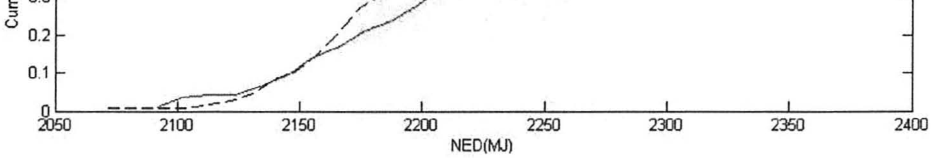

Figure 4.28: Distribution of 95/95 GRS upper bounds for NED(J)

4.6 Channel Specific Results

While the point kinetics assumption is able to produce reasonable results when applied to calculations involving the average channel or the overall HTS response to the break, the assumption of a constant spacial flux shape (implying an infinite propagation speed of local disturbances) is not very accurate for calculations of local effects. At the same time, the lack of a three dimensional neutronics model of the core[1] inhibits such calculations. The results that follow in this section are only presented as a demonstration for such calculations.

In attempting to compensate for the faster voiding rate of the hot channel, the reactivity feedback coefficient has been based purely on the average void in the hot channel, rather than the average core void, resulting in higher peak powers and a larger temperature gradient. Figure 4.29 displays the fuel centerline temperature corresponding to each of the 59 GRS runs discussed in the previous section. Header conditions for each of the 59 runs from the previous section are inputed as boundary conditions with a 40 kPa reduction in the header differential gradient, and a case is ran for the hot channel with the channel power and bundle power variable parameters with uncertainties summarized in table 4.9.

Channel Power	6740 kW	0.015
Bundle Power	820 kW	0.075

Table 4.9: Uncertainties in MCP and MBP

---

[1] Generation of such a model was deemed to be outside the scope of this work

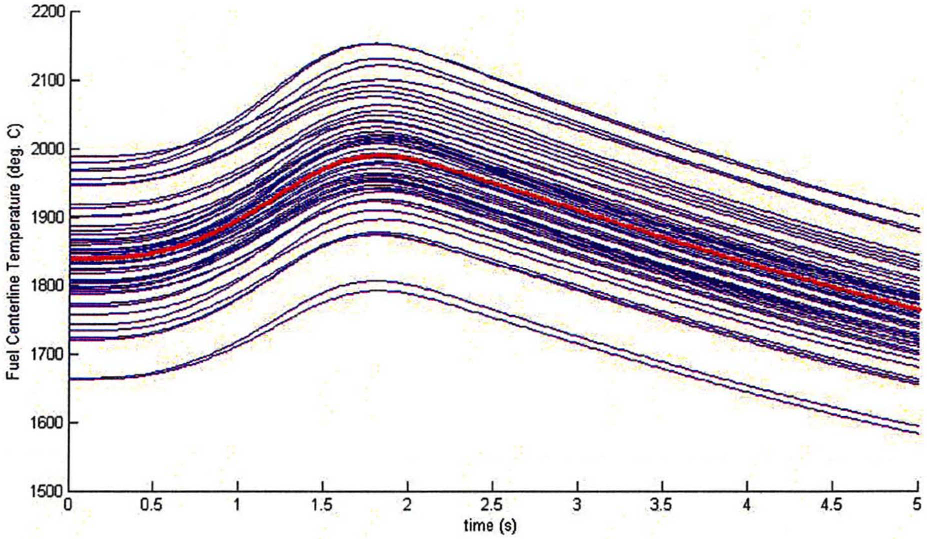

Figure 4.29: Fuel centerline temperatures (C) for the 59 GRS runs along with the reference case(red)

Chapter 5

Summary and Recommendations

A model has been constructed in RELAP5 representing a generic CANDU 900 MW plant. Uncertainties ranges and distributions for input modeling parameters and plant parameters were derived from various literature sources and plant operating data. A critical break search was performed identifying the 48% of the RIH area break size as that leading to the highest bulk energy deposition. Similar results from calculations for other CANDU reactors performed in reference [45] and [?] reinforce the consistency of the results. A parametric phenomena study was performed analyzing the reference case results and discussing the governing phenomena during the postulated accident. A ranking scheme for the input parameters was defined, and the initial PKRIT was reduced by considering parameters of high and medium importance. Calculations were made with bulk net energy deposition and peak power as the FOM using the direct Monte-Carlo method with 10000 simulations, the GRS method and the traditional LOE approach. The GRS method was found to be in well agreement with the Monte-Carlo results. The results show that considered best estimate analysis lead to a significantly higher predicted safety margins than the analysis performed using the LOE approach.

One of the main setbacks of the current analysis is the lack of a three dimensional neutronics model. While the void reactivity is the highest ranked parameter, a number of parameters identified as having medium importance in reference [45] were unable to be analyzed in the current report due to the lack of a three dimensional reactor physics model. Generation of such a model was deemed to be beyond the scope of this work. It may be of interest to perform an analysis of the given scenario using a three dimensional neutronics model coupled with RELAP5. Such a model is able to predict the local power transient. Therefore, figures of merits related to fuel channel integrity such as maximum sheath temperatures and pressure tube strain can be considered.

Bibliography

[1] Bang Y. S., Oh D. Y., Kim I.,Improvements of KINS Uncertainty Evaluation Method and Application to Simulation of L2-5 Experiment, *Korea Institute of Nuclear Safety*, May 20, 2004.

[2] Chen J.C., A Correlation for Boiling Heat Transfer to Saturated Fluids in Convective Flow, *Process Design and Development.* 5, pp. 322–327, 1966.

[3] Bromley L.A., Heat Transfer in Stable Film Boiling, *Chemical Engineering Progress*, 46, pp.221–227, 1950.

[4] Celata G.P., Cumo M., An Experimental Study of CHF under Complex and Simultaneous Transient Conditions, *Warme und Stoffubertragung*, 27, pp. 17–28 ,1992.

[5] IAEA, Thermohydraulic Relationships for Advanced Water Cooled Reactors, IAEA report, IAEATECDOC- 1203, 1991.

[6] Baek W., Kim H., Chang S., An independent assessment of Groeneveld et al.'s 1995 CHF look-up table, *Nuclear Engineering and Design*, 178, 331–337,1997.

[7] Choi K., Kim Y., Yi S., Baek W., Development of a pump performance model for an integral effect test facility, *Nuclear Egineering and Design*, 238, pp. 2614–1623, 2008.

[8] AECL, Comparison of DNGS, Bruce 'B', and CANDU6, Atomic Energy of Canada Ltd. Report.

[9] AECL, dafeedr.dat , AECL input file for NUCIRC II.

[10] Wilson D. G., Chan T. C., Goldfinch A. L., Analytical Models and Experimental Studies of Centrifugal Pump Performance in Two Phase flow, EPRI NP-170, 1977.

[11] Wilson D. G., Chan T. C., Goldfinch A. L., Analytical Models and Experimental Studies of Centrifugal Pump Performance in Two Phase flow, EPRI NP-677, 1979.

[12] Ontario Hydro, Sopht input data for Darlington NGS A Safety Analyses, OH Report No. 8043, Oct 1980.

[13] Wilks S.S. , Statistical prediction with special reference to the problem of tolerance limits, *Annals of Mathematical Statistics*, 13–4, pp. 400409, 1942.

[14] Mladin M., Dupleac, D., Prisecaru, I., SCDAP/RELAP5 application to CANDU6 fuel channnel analysis under postulated LLOCA/LOECC conditions, *Nuclear Engineering and Design*, 239, pp. 353-364, 2009.

[15] YJ Cho, GD Jeun, Assessments of RELAP5/MOD3. 2 and RELAP5/CANDU in a Reactor Inlet Header Break Experiment B9401 of RD-14M, *KOREAN NUCLEAR SOCIETY*, 2003.

[16] S Lee, K In-Goo, RELAP5 Simulation of Thermal-Hydraulic Behavior in a CANDU Reactor-Assessments of RD-14 Experiments, *Nuclear Technology*, 130 (1), pp. 18-26, 2000.

[17] Kim M., Enhancement of Safety analysis capability for CANDU-6 reactor using RELAP-CANDU/SCAN coupled code system, *Nuc. Tech.*, 156, pp. 159-167, 2006.

[18] AECL, NUCIRC I Manual, AECL document.

[19] Ontario Hydro, Darlington NGS Safety Report:Volume 1, Ontario Report Number NK38-REP-03500-001-R01, 2001.

[20] Ontario Hydro, Darlington base line reference data base da7_ss.dat, SOPHT input file for DNGS.

[21] Ontario Hydro, Sopht Source Code Subroutines in Fortran 77.

[22] Guba A., Makai M., Pal L., Chang S.H, Statistical aspects of best estimate methodI, *Reliability Engineering and System Safety*, 80, 217−232, 2003.

[23] Makai M., Pal L., Best estimate method and safety analysis II, *Reliability Engineering and System Safety*, 91, 222−232, 2006.

[24] Karassik I., Messina J., Cooper P., Heald C., PUMP HANDBOOK, McGraw-Hill, 2001.

[25] Lahey R.,Moody F.R., The Thermal-Hdraulics of a Boiling Water Nuclear Reactor, ANS Publications, 1993.

[26] RELAP5/MOD3.3 CODE MANUAL VOLUME I, Information Systems Laboratories, Idaho Falls, 2006.

[27] RELAP5/MOD3.3 CODE MANUAL VOLUME II, Information Systems Laboratories, Idaho Falls, 2006.

[28] RELAP5/MOD3.3 CODE MANUAL VOLUME III, Information Systems Laboratories, Idaho Falls, 2006.

[29] RELAP5/MOD3.3 CODE MANUAL VOLUME IV, Information Systems Laboratories, Idaho Falls, 2006.

[30] RELAP5/MOD3.3 CODE MANUAL VOLUME V, Information Systems Laboratories, Idaho Falls, 2006.

[31] SCDAP Code Manual: Matiral Properties Handbook, Information Systems Laboratories, Idaho Falls, 2006

[32] Morris A., Measurement and Instrumentation Principles, Butterworth-Heinemann, 2001.

[33] AECL, CATHENA MOD-3.5d Theory Manual, AECL document number 153-112020-STM-001

[34] Rouben B., Chapter3: Elementary Physics of Reactor Control, 6p3 course notes, 2008

[35] Garland B., Reactivity Feedback Examples, un802-2004 notes, 2004

[36] Rouben B., Kinetics, 6p03 notes, 2008

[37] Fox R.W, McDonald A.T., Pritchard P.J, Introduction to Fluid Mechanics, Wiley Press, 2006

[38] http://canteach.candu.org/library/20040711.pdf

[39] , Blachot J., Brady M.C., Filip A., Mills R.W., Weaver D.R., Status of Delayed-Neutron Data-1990,NEACRP-L-323/NEANDC-299U, OECD Nuclear Energy Agency, 1990.

[40] Crane Co., Flow of Fluids-Through Valve Fittings and Pipes, Technical paper, no. 410, 1957.

[41] Todreas N.E., Nuclear Systems Volume 2: Elements Of Thermal Design , Taylor & Francis, 1990

[42] Sermer P., Olive C., Probabilistic Approach to Compliance with Channel Power License Limits based on Optimal Maximum Uncertainty, *Proceedings of the American Nuclear Society Annual Conference*,Philadelphia, Pa, USA, June 1995.

[43] Sermer P., Hoppe F.M., A Methodology for Estimating Error in the Computed Maximum Fuel Bundle Power,22nd Annual CNS Conference, 2001

[44] Hill I., Application of best estimate methods and analysis of uncertainity methods to candu channel power, Masters Thesis, McMaster University. Dept. of Engineering Physics., 2006

[45] Blake L., Vecchiarelli J, Canadian Utility Application of Best Estimate And Uncertainty Analysis Pickering NGS B Power Pulse BEAU Analysis,Presentation to SUNCOP, 2007.

[46] An Overview of Westinghouse Realistic Large Break LOCA Evaluation Model

[47] Leung K., CFD of Advanced passive Moderator Systems, Masters Thesis, McMaster University. Dept. of Engineering Physics., 2006

[48] Glaeser H., GRS Method for Uncertainty and Sensitivity Evaluation of Code Results and Applications, *Science and Technology of Nuclear Installations*, Volume 2008.

[49] Fauske, H. K., The Discharge of Saturated Water Through Tubes, *Chem Engr. Prog Symp Ser*, 61:210, 1965.

[50] Fauske, H. K., Contribution to the Two-phase One-component Critical Flow, Argonne National. Laboratory Report ANL-6633, 1962.

[51] BAILEY J. F.,Metastable flow of saturated water, *Trans. ASME*, 73, 1109-1116 ,1951.

[52] McAdams H. W., Frost T. H., Heat Transfer for Water Flowing Inside Pipes, *Refrigerating Engineering*, 10, 1924.

[53] R.E. Henry, H.K. Fauske, The Two-Phase Critical Flow of One-Component Mixtures in Nozzles, Orifices, and Short Tube, *Transactions of ASME, Journal of Heat Transfer*, 93, pp. 179–187, 1971.

[54] Kahn H., Multiple Quadrature and Monte Carlo Methods, Mathematical Methods for Digital computers, volume 1, John Wiley and Sons, 1967.

[55] Tangren R.F., Dodge C.H., Seifert H.S., Compressibility Effects in Two Phase Flow, *Journal of Applied Physics*, 20, 1949.